ORNL/SPR-2022/2672

Evaluation of the Effect of Burnup Acceleration on UO_2 Microstructure Evolution

A. Cheniour
K. Godsey
Z. Wallen
T. Ulrich
J. M. Harp
C. M. Petrie
N. A. Capps

October 2022

OAK RIDGE National Laboratory

ORNL IS MANAGED BY UT-BATTELLE LLC FOR THE US DEPARTMENT OF ENERGY

ORNL/SPR-2022/2672

Advanced Fuels Campaign Milestone Report: M3FT-22OR020205031

Evaluation of the Effect of Burnup Acceleration on UO_2 Microstructure Evolution

A. Cheniour
K. Godsey
Z. Wallen
T. Ulrich
J. M. Harp
C. M. Petrie
N. A. Capps

October 2022

Prepared by
OAK RIDGE NATIONAL LABORATORY
Oak Ridge, TN 37831
managed by
UT-Battelle LLC
for the
US DEPARTMENT OF ENERGY
under contract DE-AC05-00OR22725

CONTENTS

LIST OF FIGURES

LIST OF TABLES

ABBREVIATIONS

AFQ accelerated fuel qualification

CNT classical nucleation theory

FP fission product

HBS high-burnup structure

HFIR High Flux Isotope Reactor

HFIRCON HFIR Controller

LWR light-water reactor

MCNP Monte Carlo N-Particle

MOOSE Multiphysics Object-Oriented Simulation Environment

ORNL Oak Ridge National Laboratory

PWR pressurized water reactor

ACKNOWLEDGMENTS

This work was supported by the Advanced Fuels Campaign within the US Department of Energy (DOE) Office of Nuclear Energy (NE). This research made use of Idaho National Laboratory computing resources, which are supported by DOE NE and the Nuclear Science User Facilities under Contract No. DE-AC07-05ID14517.

ABSTRACT

Accelerated fuel qualification (AFQ) is a methodology by which new nuclear fuels are developed in an accelerated time frame compared with historical fuel qualification approaches. AFQ generally relies on high-fidelity physics-based modeling and simulation tools to adequately describe fuel performance as well as on revolutionary methods to accelerate burnup accumulation and collect relevant data more quickly. This report summarizes the use of advanced fuel modeling and simulation tools to evaluate microstructures from commercially irradiated fuel and microstructures from proposed MiniFuel irradiations, in which burnup accumulation is accelerated while prototypic temperature conditions are maintained. In this milestone, we used the mesoscale fuel performance code MARMOT to model the evolution of irradiated UO_2 microstructures and their potential restructuring at high burnup. The simulation conditions were informed by BISON models of both commercially irradiated fuel and MiniFuel. A first set of simulations investigated the recrystallization behavior of fully dense microstructures and showed full recrystallization at burnups as low as 52 MWd/kgU at 950°C. However, these simulations did not account for the presence of fission gas bubbles (predicted by BISON). Therefore, a second set of simulations including fission gas bubbles was performed and indicated that at the lowest temperature considered (650°C), the porous UO_2 microstructures have the highest total Gibbs free energies and are likely to recrystallize earlier than higher temperature cases (800 and 950°C), which agrees with high-burnup fuel characterization data. The results also showed that at lower temperature (650°C), the total free energies of the PWR fuel and MiniFuel microstructures are not significantly different. However, at the highest temperature (950°C), MiniFuel microstructures have a lower free energy than that of the PWR fuel microstructure. The competing effects between the temperature-dependent grain nucleation rate and the reduction of the free energy of the microstructure at higher temperature as a result of diffusion indicated that restructuring may occur at even higher temperatures than those considered in this study. In addition to the microstructure evolution modeling efforts, the burnup gradient across a single fuel specimen was also considered. This evaluation was for the VXF-15 position of the High Flux Isotope Reactor (HFIR) using the code suite HFIRCON, which was developed to automate the workflow for evaluating targets and fuel as they are irradiated in HFIR. The burnup gradient evaluation showed a dependence on both the axial and radial locations within the specimen, with a maximum difference of 1.7 between the inner and outermost radial layers. This relationship was further supported by considering the fission product speciation with respect to location within the specimen, which showed a higher concentration of ^{239}Pu, ^{240}Pu, and ^{241}Pu on the outer radial locations of the specimen than the center. The findings of the burnup and speciation evaluation show that some amount of self-shielding is occurring in the specimen when irradiated in the high-flux environment of HFIR; however, this impact is more pronounced for natural uranium when compared to 6% enrichment due to the higher ratio of ^{238}U in the specimen. Further analyses are required to understand the sensitivity of this gradient to spatial mesh and enrichment of the specimen.

1. INTRODUCTION

The process to develop and qualify nuclear fuel for commercial application requires fundamental material development and characterization; out-of-pile testing on unirradiated materials; integral fuel rod irradiations, testing, and postirradiation examinations; and transient analyses [1, 5]. The historical approach depends on the generation of large empirical data sets and series of integral fuel rod irradiations, and this approach ultimately takes approximately 20 years—or sometimes longer—to acquire data through extensive sequential testing. Thus, the qualification and eventual deployment of new fuel systems constitute a long and drawn-out process. Additionally, the urgent need to deploy advanced reactor technologies globally and in the United States to replace the aging light-water reactor (LWR) fleet requires new, faster, and more efficient fuel development and qualification.

Accelerated fuel qualification (AFQ) is a methodology by which new nuclear fuels are developed in an accelerated time frame compared with historical fuel qualification approaches. AFQ generally relies on high-fidelity physics-based modeling and simulation tools to adequately describe fuel performance as well as on revolutionary methods to accelerate burnup accumulation and collect relevant data more quickly. This work used advanced fuel modeling and simulation tools to evaluate microstructures from commercially irradiated fuel and microstructures from proposed MiniFuel irradiations, in which burnup accumulation is accelerated while prototypic temperature conditions are maintained. The comparison between both microstructure sets revealed the applied models' prediction of the effects of accelerated burnup on microstructure evolution. These results support future reliance on predictive models to guide future experiments and potentially reduce the number of required experiments.

Detailed data from high-burnup microstructure analyses are available in the literature [6]. Additionally, fuel rod irradiation conditions are available for the high-burnup microstructures reported in the literature [6]. In this study, BISON simulations provided local fuel temperatures as well as burnup and fission rate accumulation as a function of time and radial location for subsequent simulation using the mesoscale fuel performance code MARMOT. MARMOT was then used to evaluate the radial microstructural evolutions in commercial nuclear fuel. The MARMOT results were compared with the high-burnup microstructure data from commercially irradiated nuclear fuel to ensure consistency.

MiniFuel irradiation capsules offer an opportunity to decouple fuel temperature from fission rate [7]. This decoupling allows fuel to accumulate burnup at a faster rate while maintaining a constant fuel temperature. Using MARMOT, this work assessed microstructure evolutions of irradiated UO_2 under accelerated burnup conditions that could be achieved in a future MiniFuel irradiation. Fuel temperatures in the MARMOT simulation were intended to be similar to and consistent with local temperature and burnup conditions calculated from the BISON simulations proposed earlier in this work. This allowed for a comparison between the MARMOT accelerated burnup microstructure predictions and the MARMOT microstructure predictions of commercially irradiated fuel under similar temperature and burnup conditions.

This milestone study also explored some additional phenomena that could affect experiments designed to accelerate fission rate to reach high burnup (i.e., MiniFuel). Current simulations assume that MiniFuel samples will uniformly accumulate burnup; however, significant spatial variations in burnup could exist because of self-shielding effects. Therefore, a neutronic self-shielding analysis is needed to verify uniform burnup accumulation or to determine the effect of self-shielding. Additionally, MiniFuel accumulates burnup by fissioning plutonium bred from neutron capture in uranium instead of utilizing highly enriched uranium to accelerate burnup accumulation. This burnup accumulation via plutonium fission ultimately

modifies the fission product content in MiniFuel compared to that of commercially irradiated high-burnup fuel. Thermochemical calculations must be performed to quantify the difference in fission product speciation between LWR irradiated fuel (75% ^{235}U fissions) vs. MiniFuel irradiations (95% ^{239}Pu fissions). That ^{239}Pu fission in high-burnup fuel significantly increases is an additional benefit of thermochemical calculations, and the results of such analyses could provide valuable information on LWR fuel with a burnup greater than 62 GWd/mtU, where ^{239}Pu fission becomes more dominant.

2. MARMOT ASSESSMENT OF HIGH-BURNUP MICROSTRUCTURES

The microstructure of commercial UO_2 fuels undergoes temperature- and burnup-dependent changes, such as the nucleation and growth of fission gas bubbles, as well as grain subdivision and pore formation at the periphery of the fuel pellet [8, 9]. Characterization of high-burnup UO_2 fuel showed that its microstructural features are highly dependent on the radial position within the pellet [6]. In particular, the high-burnup structure (HBS) or rim structure at the fuel periphery shows depleted submicrometer grains and micrometer-size pores filled with fission gas [10]. HBS is of particular interest because it affects fuel performance by potentially retaining fission gas [11], decreasing the fuel thermal conductivity locally [9] and increasing the softness of the material [9, 12]. Characterization data show that recrystallization and polygonization are potential mechanisms behind HBS because both low- and high-angle grain boundaries are observed in the structure [9, 13].

Ongoing experimental efforts take advantage of the recent MiniFuel concept to provide a separate-effects analysis of fuel performance and microstructural evolution in accelerated burnup conditions. MiniFuel can be irradiated at an independently chosen temperature and fission rate and does not require increased fuel enrichment, which represents a unique opportunity to reproduce the mechanisms happening at specific radial regions of a commercial fuel pellet at lower cost and reduced manufacturing efforts. A potential application of MiniFuel would be to obtain HBS formation at low temperatures and high fission rates, both of which are representative of the irradiation conditions at the pellet rim region. This potential application raises the question of the effect of accelerated burnup conditions on the microstructural evolution at high burnup. One anticipated effect is an enhanced fission gas diffusion, which is sensitive to the fission rate [14].

When supported by irradiation data, modeling and simulation can help to elucidate the mechanisms behind HBS formation and to potentially predict the necessary burnup and temperature conditions for grain subdivision. Modeling the formation of HBS is inherently a complex multiscale problem that relies on modeling radiation damage and fission gas behavior, nucleating new grains and bubbles, and evaluating the development of dislocation loops in the structure. Modeling grain subdivision typically uses recrystallization models, which can use classical nucleation theory (CNT) to generate smaller grains [15] as well as intergranular fission gas bubbles. Various approaches are available in the literature [10, 13, 16–19]. In their work, Abdoelatef et al. [18] applied a free energy–based model using the phase field method to stochastically form new grains at grain boundaries and a temperature set to 1,200 K. The bulk energy results from the accumulation of dislocations, which uses an empirical model of the dislocation density in UO_2 [20] and fission gas atoms [18]. A different phase field approach is used in Smith et al. [13] to model the recrystallization of U–Mo grains at high burnup, where nucleation is enforced at a critical dislocation density. Although the model details are only briefly given in [13], the approach seems to capture the fully recrystallized structure at high burnup. A similar model was previously employed in U–Mo to investigate fuel swelling caused by intergranular gas bubbles in the recrystallized structure [17].

This study developed and applied phase–field recrystallization and fission gas bubble growth models at different radial positions of an LWR commercial UO_2 fuel pellet. The same model was applied to MiniFuel at the same temperatures but with higher fission rates that can be applied to UO_2 MiniFuel in the High Flux Isotope Reactor (HFIR) at Oak Ridge National Laboratory. The models were informed by engineering-scale fuel performance simulation data of both LWR fuel and MiniFuel to provide a realistic set of irradiation conditions. This report starts by providing a description of the preliminary fuel performance simulations and the phase–field models in Section 2.1. The simulation results are shown in

Section 2.2 for two cases: (i) a fully dense structure and (ii) a porous structure. This study also discusses the limitations in these models and provides recommendations for future work in Section 2.2.

2.1 MODELING APPROACH

The engineering-scale fuel performance code BISON [21] was used to simulate steady-state irradiation conditions for both UO_2 MiniFuel in HFIR and commercial UO_2 fuel in a pressurized water reactor (PWR). The purpose of these simulations was to obtain realistic simulation conditions at the microstructural level using the mesoscale fuel performance finite-element code MARMOT. In particular, fission rate, porosity, and fission gas content were extracted from BISON simulations at chosen sets of temperature and burnup. This study investigated temperatures ranging from 650°C to 950°C at an initial average burnup of approximately 40 MWd/kgU. These conditions were chosen to study the microstructural evolution of irradiated UO_2 at high burnup and relatively low temperatures compared to a typical PWR fuel centerline temperature. The initial burnup was selected to be far enough from the recrystallization onset [9]. In this section, the computational approach to study high-burnup microstructural features and evolution is detailed, starting from the preliminary BISON simulations to modeling an irradiated UO_2 microstructure in MARMOT.

2.1.1 Fuel Performance Models

2.1.1.1 Commercial UO_2 Fuel

PWR fuel was modeled using a 2D axisymmetric smeared UO_2 pellet model in BISON using realistic conditions taken from Figure 16 of Capps et al. [22]. The model was previously described and used in Cheniour et al. [23]. It includes ZIRLO® cladding and a gap separating the cladding from the smeared pellet. The pellet outer radius is 0.4096 cm. The fuel rod dimensions are based on the Westinghouse AP1000 Design. The linear heat rate, temperature, and pressure boundary conditions, as well as the axial peaking factor, are obtained from realistic three-cycle PWR core data. The initial fuel porosity was set to 5% and the grain size to 10 μm. The radial profiles of properties of interest were extracted at an average burnup of 40 MWd/kgU and temperatures of 650°C (case 1 in this study), 800°C (case 2), and 950°C (case 3), which correspond to different radial positions within the fuel pellet. This set of temperatures was chosen to accommodate limitations in the phase-field model used in MARMOT for microstructural evolution simulations, which will be discussed in Section 2.2. The radial temperature profile at 40 MWd/kgU and rod midheight are shown in Figure 1.

Table 1 shows the BISON results of interest for the MARMOT models for each chosen temperature at 40 MWd/kgU burnup. These conditions were then used to set up MARMOT simulations of PWR fuel microstructure under irradiation, which are discussed in Section 2.2. These simulations assumed a constant temperature. However, fuel temperature is subject to potential variations, such as variation caused by changes in fuel density over time.

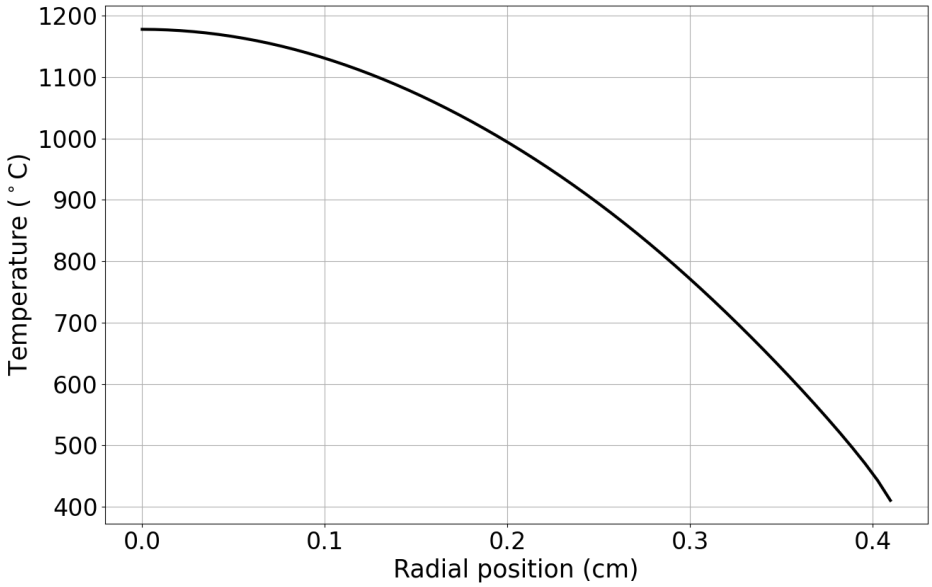

Figure 1. PWR UO_2 fuel radial temperature profile at a burnup of 40 MWd/kgU calculated using BISON.

Table 1. BISON simulation results for PWR UO_2 fuel

Case	1	2	3
Temperature (°C)	650	800	950
Radial position (cm)	0.34	0.28	0.20
Local burnup (MWd/kgU)	42	41	41
Fission rate ($\times 10^{19}$ fissions/(m^3s))	1.338	1.309	1.305
Fission gas produced ($\times\ 10^{-4}$ mol/cm^3)	4.91	4.91	4.91
Intragranular fission gas ($\times\ 10^{-4}$ mol/cm^3)	4.73	4.73	4.70
Local porosity (%)	4.4	4.6	5.1

Table 2. BISON simulation results for UO_2 MiniFuel

Case	1	2	3	4	5	6
Temperature (°C)	650	800	950	650	800	950
Burnup (MWd/kgU)	40	40	40	40	40	40
Fission rate ($\times 10^{19}$ fissions/(m^3s))	3.21	3.21	3.21	6.42	6.42	6.42
Fission gas produced ($\times 10^{-4}$ mol/cm^3)	4.82	4.82	4.82	4.82	4.82	4.82
Intragranular fission gas ($\times 10^{-4}$ mol/cm^3)	4.79	4.79	3.97	4.75	4.75	4.01
Porosity (%)	4.7	4.9	5.1	5.2	5.4	5.6

2.1.1.2 UO_2 MiniFuel

To complement the fuel performance simulations of PWR fuel, a set of MiniFuel simulations were performed using approximated HFIR conditions using BISON. The MiniFuel simulations used the geometry and mesh described in Cheniour et al. [24]. Again, three temperature cases were studied: 650°C, 800°C, and 950°C at a burnup of 40 MWd/kgU. Because the linear heat rate depends on the ^{235}U enrichment used in the MiniFuel specimen and the experiment position [7], two fission rates were used in the MiniFuel simulations to evaluate the effect of different fission rates on the fuel microstructure. They equate to 8.8 and 17.6 kW/m if the fission rates were applied to a full-size LWR pellet. These fission rates correspond to approximately 93 and 186 W/g fission heating, respectively, which are close to the fission heating at the inner small VXF positions in HFIR. A total of six cases were considered for MiniFuel. The initial porosity and grain size were set to the same values as in the PWR case. Table 2 provides the BISON simulation results for UO_2 MiniFuel.

2.1.2 HBS Formation Model

The phase–field method was used to model a polycrystalline structure representative of irradiated UO_2 at the microstructural scale. Applications of this method, such as modeling grain growth, void or bubble growth, and spinodal decomposition, are available in the literature [25–27]. Phase–field models of radiation damage in nuclear materials were also previously developed in other works [28–30]. These models vary in complexity (e.g., multiscale modeling, types of defects considered) and limitations. In this study, a radiation damage phase–field model informed by CNT was used to model the recrystallization of UO_2 grains at high radiation dose. Initially, this model was applied to a fully dense microstructure. In a second set of simulations, a number of intergranular bubbles were added according to the fuel porosity calculated using BISON.

2.1.2.1 Phase–Field Model

This work uses the grand potential formulation of the phase–field model described by Aagesen et al. [31]. The grand potential density is obtained through a Legendre transform of the Gibbs free energy density [32]. For simplicity, only the free energy–based formulation is presented in this section. The Allen–Cahn

equation was used to model grains or fission gas bubbles:

$$\frac{\partial \eta_i}{\partial t} = -L_i \frac{\delta F}{\delta \eta_i}, \tag{1}$$

where η_i is the order parameter or phase field representing phase i such that η_i=1 inside the phase, η_i=0 outside the phase, and $0 < \eta_i < 1$ at the interface; t is time; L_i is the phase mobility; and F is the total Gibbs free energy. In addition to grains and bubbles, the evolutions of fission gas atoms and uranium vacancies were modeled using the Cahn–Hilliard equation:

$$\frac{\partial c_j}{\partial t} = \nabla \cdot M_j \nabla \frac{\delta F}{\delta c_j} + P_j, \tag{2}$$

where c_j is the atomic fraction or concentration of species j, M_j is the corresponding chemical mobility, and P_j is the production rate. The total free energy is given by:

$$F = \int (f_{int} + f_{chem} + f_{disloc})\, dV \tag{3}$$

where f_{int} is the interfacial energy density taken from Eqs. (2–4) in Aagesen et al. [31], f_{chem} is the chemical free energy density caused by the accumulation of gas atoms and uranium vacancies, and f_{disloc} is the free energy density caused by dislocations. For simplicity, the elastic energy was not modeled in this work. Both Eqs. (1) and (2) use the variational derivative of F:

$$\frac{\delta F}{\delta \eta_i} = \frac{\partial f_{int}}{\partial \eta_i} + \frac{\partial f_{chem}}{\partial \eta_i} + \frac{\partial f_{disloc}}{\partial \eta_i} - \kappa_i \nabla^2 \eta_i, \tag{4}$$

where κ_i is the gradient energy coefficient, expressed as:

$$\kappa_i = \frac{3}{4} \sigma_i l_{int} \tag{5}$$

where σ_i can, for instance, be the grain boundary energy or a surface energy depending on the interface's nature, and l_{int} is the interfacial width. For the bubble–UO_2 interface, this study considered that the interfacial energy is equal to the UO_2 surface energy, which is approximately two times higher than the UO_2 grain boundary energy [33].

The phase–field model parameters are typically derived from physical quantities such as the grain boundary energy and mobility for the phase mobility L_i of grain i. For the bubble phase η_b, the phase mobility was chosen to allow a reasonable time step while still limiting the interface mobility by diffusion, as done in Aagensen et al. [30]. The grain phase mobility is expressed as

$$L_i = \frac{4}{3} \frac{M_{gb}}{l_{int}}, \tag{6}$$

where M_{gb} is the temperature-dependent grain boundary mobility. The bubble–UO_2 interface mobility was set to $100 \times L_i$. The chemical mobility M_j follows the equation

$$\frac{\partial^2 f_{chem}}{\partial c_j^2} M_j = D_j, \tag{7}$$

where D_j is the atomic diffusion coefficient of species j. The atomic diffusion coefficients were multiplied by 100 at interfaces to obtain faster diffusion at grain boundaries and interfaces between bubbles and grains. The fission gas is assumed to be xenon only; therefore, its diffusivity follows the expression by Turnbull [14]. The uranium vacancy diffusion coefficient is taken from Matzke [34].

The interfacial energy density takes the form

$$f_{int} = \mu f(\eta_i, \eta_b), \tag{8}$$

where μ is a constant derived as

$$\mu = 6\frac{\sigma_i}{l_{int}}. \tag{9}$$

The chemical free energy density uses the ideal solution model such that

$$f_{chem} = h_a f_a + h_b f_b, \tag{10}$$

where h_a and h_b are switching functions [31] of the UO_2—h_a for the matrix phase a and h_b for the fission gas bubble phase b, and f_a and f_b are the corresponding chemical energy densities. The chemical free energy densities are defined as

$$f_a = \frac{1}{V_a}\sum_j [E_{f_j} c_j + k_B T(c_j ln(c_j) + (1 - c_j) ln(1 - c_j))], \tag{11}$$

$$f_b = \frac{1}{2}\sum_j [A_j (c_j - c_{j_{eq}})^2], \tag{12}$$

where V_a is the uranium atomic volume, E_{f_j} is the formation energy of species j, k_B is Boltzmann's constant, T is temperature, A_j is a parabolic free energy coefficient, and $c_{j_{eq}}$ is the equilibrium concentration.

The ideal solution model used in this work also follows the approach of Aagesen et al. [30], which assumes that gas atoms and uranium vacancies do not occupy the same lattice site. This approach was chosen because the current grand potential formulation does not allow obtaining a Legendre transform analytically for a multicomponent system on a single lattice. However, for site conservation purposes, the equation should be modified in future work to account for potential gas atoms on uranium lattice sites by integrating a numerical solution of the corresponding grand potential function.

A parabolic fit of the Van der Waals gas Helmholtz energy density equation, f_b, follows the approach of Aagesen et al. [30]. A parabolic energy density approximation significantly improves the numerical convergence to the solution because it is continuously differentiable and allows small numerical errors in the solution without significantly affecting the convergence. The A_j coefficients and the equilibrium concentrations $c_{j_{eq}}$ were determined for each temperature considered in this study. A_j was set to the same value for both gas and vacancy contributions to f_b. The value was high enough to ensure that at equilibrium, the gas concentration in the bubble phase was set to the minimum of the Van der Waals gas energy density at a specific temperature. In the bubble phase, the sum of the concentrations of gas (c_g) and vacancies (c_v) is equal to 1.

The dislocation free energy density is modeled using the equation

$$f_{disloc} = \frac{1}{2} G b^2 \rho_d, \tag{13}$$

where G is the UO_2 shear modulus, b is the length of the Burgers vector, and ρ_d is the dislocation density. Similarly to the HBS formation model in [18], the empirical relationship between ρ_d [m/m^3] and burnup β [MWd/kgU] was used:

$$log(\rho_d) = 2.2 \times 10^{-2}\beta + 13.8, \tag{14}$$

which was obtained from dislocation density measurements in the peripheral region of a fuel pellet irradiated in a boiling water reactor [20]. This expression was used in this study as a substitute to dislocation density calculations based on defect accumulation, which typically use the rate theory [16, 19]. The dislocation density is assumed to be uniform everywhere in the domain outside of bubbles and nucleated grains, where it was set to zero.

This model used the phase–field module of the Multiphysics Object-Oriented Simulation Environment (MOOSE) framework, which is used by MARMOT. The Grain Tracker algorithm [35] was used to reduce the computational cost by associating an order parameter with potentially more than a single grain when the number of grains exceeds the number of order parameters. This model is particularly useful in recrystallization problems, where the number of grains can rapidly increase, without the need for additional order parameters. This model drastically reduces the number of degrees of freedom in the simulation.

2.1.2.2 Nucleation Model

The discrete nucleation algorithm available in MOOSE was used to generate new circular grains based on a provided nucleation probability through direct modification of a reserved order parameter. Nucleation was assumed to occur at a specified rate, which is a function of the nucleation driving force and temperature. The driving force Δf is a result of the dislocation energy and the energy caused by gas atoms and uranium vacancy accumulation in the matrix. The CNT was used to compute the critical nucleation free energy G^* [15]:

$$\Delta G^* = \frac{\pi\gamma^2}{\Delta f}, \tag{15}$$

where γ is the free energy of the interface, expressed as:

$$\gamma = \frac{\sqrt{\kappa_i \mu}}{3\sqrt{2}}. \tag{16}$$

The CNT also provided the critical radius r^*, where the derivative of the free energy of a circular particle with respect to the radius is equal to zero. However, because r^* can be very small, a new nucleus can require a very refined mesh at the nucleation site. To mitigate this issue, a radius was set large enough to permit a reasonable mesh refinement level and thus a significantly lower computational cost. This constitutes a limitation of the proposed nucleation approach.

The nucleation rate J was calculated as follows:

$$J = K \exp\left(-\frac{\Delta G^*}{k_B T}\right), \tag{17}$$

where K is the rate constant. A similar Arrhenius equation was used by Takaki et al. [36] in their nucleation rate model. K was set to a value that limits the number of nucleated grains every time step to a

reasonable number to avoid significant overlapping between preexisting nuclei and new nuclei, which is not prohibited in MOOSE's discrete nucleation algorithm. This nucleation rate calculation was performed on a trial-and-error basis. In the discretized simulation domain, the nucleation probability P is taken as [15]

$$P(t) = 1 - \exp(-J\Delta t). \tag{18}$$

The issue of possible overlaps between nuclei was partially solved by setting conditions in the nucleation probability function such that

1. if a preexisting nucleus covers the current element, then set P and the dislocation density to zero, and
2. the maximum value that P can take is 10^{-5} to avoid a large number of new nuclei (which would result in many overlaps) at a single time step.

Although these conditions would reduce overlaps, nucleating new grains in the vicinity of preexisting nuclei would still be possible, which is another limitation of this approach. The first condition is a natural assumption in a recrystallization problem, where new grains are considered defect-free. Following the approach of [13, 17], nucleation was set to occur at interfaces only. This approach inherently creates overlaps after the first layer of new grains is produced at the grain boundaries of the initial grains.

2.1.2.3 Simulation Setup

All simulations were performed in 2D with a domain size of 15×15 μm^2. The basic mesh was set to 100×100 first-order quadrilateral elements, and four levels of mesh refinement were added at the initialization of the domain at interfaces only, such that the smallest element size was 9.375 nm. Mesh adaptivity was then used throughout the simulation run on all order parameters as well as any new nuclei. The number of grain order parameters was between 9 and 14, depending on the simulation's needs. An additional reserved order parameter was used to include new nuclei before remapping them between the grain order parameters, which is enabled through Grain Tracker. The interfacial width l_{int} was set to 70 nm to obtain at least seven elements across the interface. Periodic boundary conditions were used in all the simulations.

The radius of a new nuclei was set to 675 nm, which is larger than the size of typical submicrometer grains in HBS reported in the literature [6, 20]. However, this was necessary to reduce the memory usage because each new nucleus induces further mesh refinement, which increases the number of degrees of freedom in the simulation. The initial conditions of c_g and c_v (or their respective chemical potentials in the grand potential formulation) in the bulk material were obtained from the preliminary BISON simulations. When considering a fully dense microstructure, c_g was calculated based on the total fission gas produced. In a porous microstructure, c_g was obtained from the intragranular fission gas. In all cases, c_v was assumed to be 3× higher than c_g in the bulk material. In the bubble phase, these concentrations were set to their equilibrium values. The initial polycrystalline structure was obtained using a Voronoi tessellation with three initial grains of approximately 10 μm in size. Both initial microstructures are shown in Figure 2. The initial bubble size and number could vary depending on the porosity calculated by BISON. The bubble size was mostly around 800 nm, and the bubble number varied between 20 and 25. Bubble nucleation was not modeled in this work for simplicity; however, the discrete nucleation algorithm can also be applied for bubble nucleation.

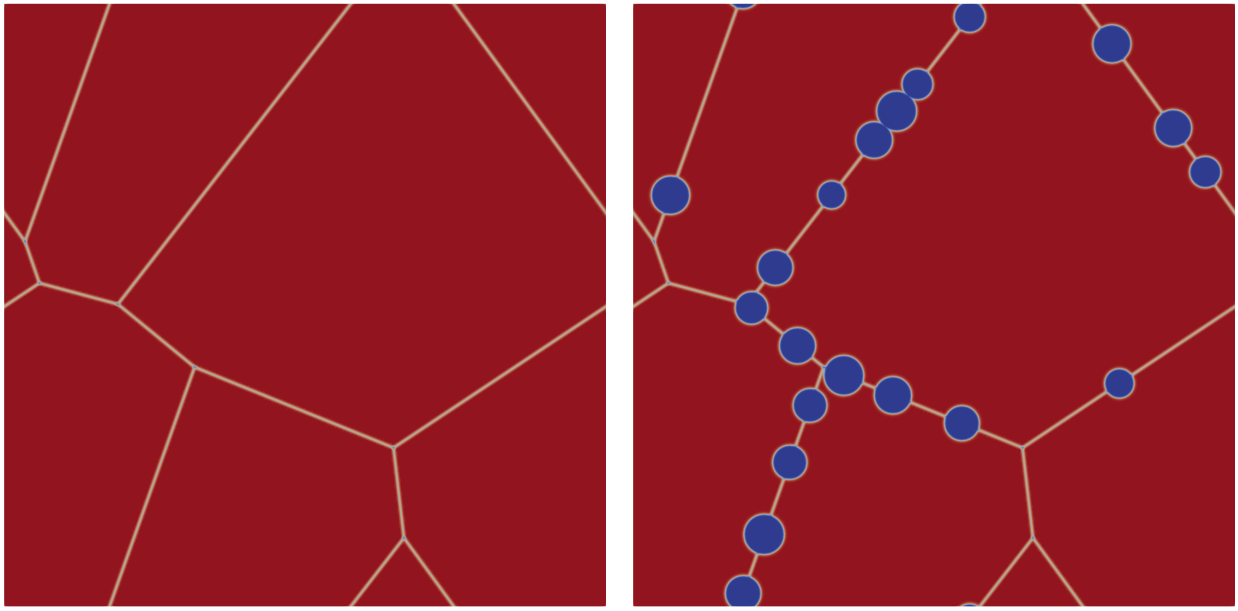

(a) Fully dense microstructure. **(b) Example porous microstructure.**

Figure 2. Initial UO_2 polycrystalline microstructures (domain size: 15×15 µm^2).

The fission rate density $\dot{F}$ also varied depending on the considered case. The burnup β was calculated as

$$\beta(t) = 950 \frac{\dot{F}}{N_U} t, \tag{19}$$

where N_U is the ^{235}U density. The defect production rate P_j was assumed uniform and was derived from the fission rate density as follows:

$$P_g = y V_a \dot{F}, \tag{20}$$

where y is the fraction of fission gas among fission products set to $y = 0.2156$ [30].

The initial time step was set to 1 s, and the following time steps were allowed to increase to $10^6 s$. The simulation start time was adjusted, depending on the fission rate, to start at a burnup of approximately 40 MWd/kgU. All simulation parameters used in this work are shown in Table 3.

2.2 RESULTS AND DISCUSSION

2.2.1 Fully Dense Microstructure

In their work, Smith et al. [13] initially applied the discrete nucleation algorithm to a polycrystalline system without fission gas bubbles. Their nucleation model used a critical dislocation density to determine the starting point of recrystallization based on experimental observations. This concept was also used by Takaki et al. [36]. In this study's model, however, the critical energy was calculated at each time and location considered, following the CNT-based model in [15]. Temperature was expected to play an

Table 3. Simulation parameters

Parameter	Value	Reference
Initial grain number (—)	3	—
Initial grain size (μm)	≈ 10	—
Nucleated initial grain radius (nm)	675	—
^{235}U density N_U (atoms/cm^3)	2.325×10^{22}	—
Nucleation rate constant K (/s)	10^{13}	—
U vacancy formation energy E_{f_v} (eV)	3.3	[37]
Xe incorporation energy E_{f_g} (eV)	3.88	[38]
U atomic volume V_a (nm^3)	0.04092	[39]
Parabolic energy coefficients $A_g = A_v$ (eV/nm^3)	200	—
Grain boundary mobility activation energy Q (eV)	2.77	[40]
Grain boundary mobility rate constant M_0 (nm^2/eVs)	1.4759×10^{9}	[40]
UO_2 shear stress G (GPa)	73	[20]
UO_2 Burgers vector length (nm)	0.39	[20]
Grain boundary energy σ_{gb} (J/m^2)	1.4125	[41]
Interfacial width l_{int} (nm)	70	—
U vacancy diffusion coefficient D_v (nm^2/s)	$2\times10^{11}\exp(-2.4/k_B/T)$	[34]
Xe diffusion coefficient D_g (nm^2/s)	$(7.6\times10^{-10}\exp(-35250/T)$ $+1.14\times10^{-25}\sqrt{\dot{F}}\exp(-13700/T)$ $+2\times10^{-40}\dot{F})\times10^{18}$	[14]

important role not only because the total free energy is temperature-dependent but also because of the Arrhenius expression used for the nucleation rate.

Here, an example recrystallization result is shown in Figure 3 for MiniFuel case 3 (950°C) at two burnup levels. Figure 3a shows the initiation of nucleation at grain boundaries at 49 MWd/kgU, which then rapidly expands to almost the entirety of the domain at 53 MWd/kgU, as shown in Figure 3b. The corresponding polycrystalline structure is shown in Figure 4. New grains are initially circles, and the phase–field grain growth model (Eq. 1) drives grain boundaries to take a shape that reduces the system's free energy, which, in this case, resulted in the polycrystalline structure shown in Figure 4. Additionally, based on the free energy contributions (Eq. 3), the total free energy for each temperature is expected to be nearly the same at a given burnup. The free energy increase caused by dislocations is solely dependent on burnup and the gas atom, and uranium vacancy production rates depend only on the fission rate. The PWR cases have slightly different local burnups than those of the MiniFuel cases.

The simulation results were plotted as the recrystallization volume fraction as a function of burnup in Figure 5 to show the effects of each simulation condition on recrystallization. The figure shows three main regions that correspond to the three temperatures applied in this study. Higher temperature cases initiate recrystallization earlier than lower temperature cases. The figure shows that at the highest temperature, recrystallization occurs very rapidly around a burnup of 50 MWd/kgU in all three cases: PWR case 3 and MiniFuel (mFuel) cases 3 and 6. This rapid recrystallization results in a nearly fully recrystallized structure. The midtemperature cases also show similar recrystallization trends initially around 55 MWd/kgU, and the same applies to the low-temperature cases around 63 MWd/kgU. The recrystallization rates at mid and low temperatures seem to vary with fission rates; however, this variation is most likely explained by another

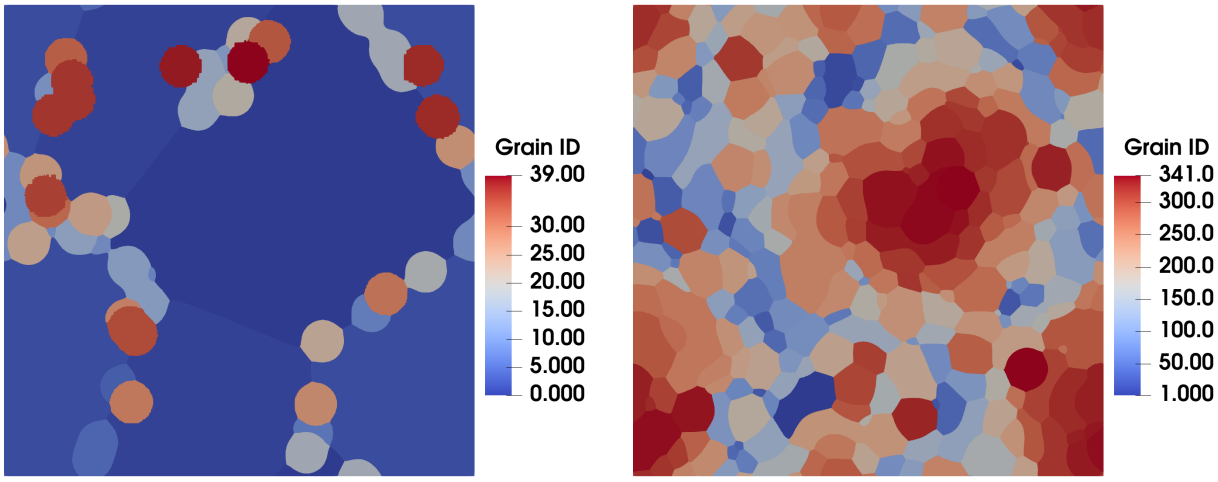

(a) β **= 49 MWd/kgU.** **(b)** β **= 53 MWd/kgU.**

Figure 3. Recrystallization at two burnups for MiniFuel case 3 (T **= 950°C).**

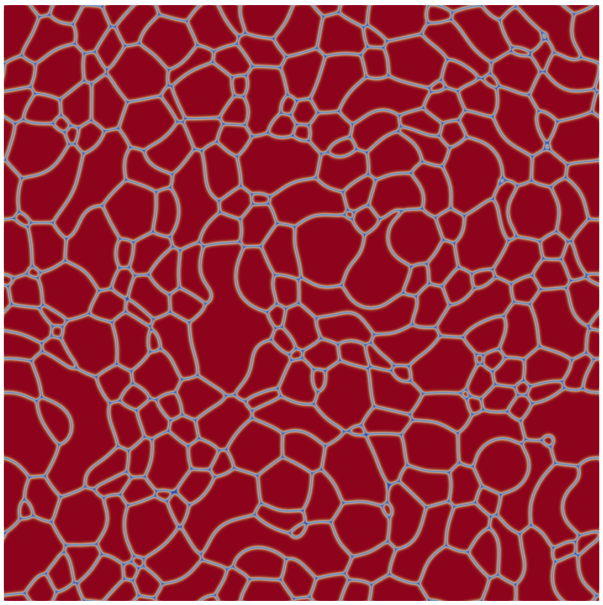

Figure 4. Near-full restructuring in UO_2 **MiniFuel case 3 (**T **= 950°C).**

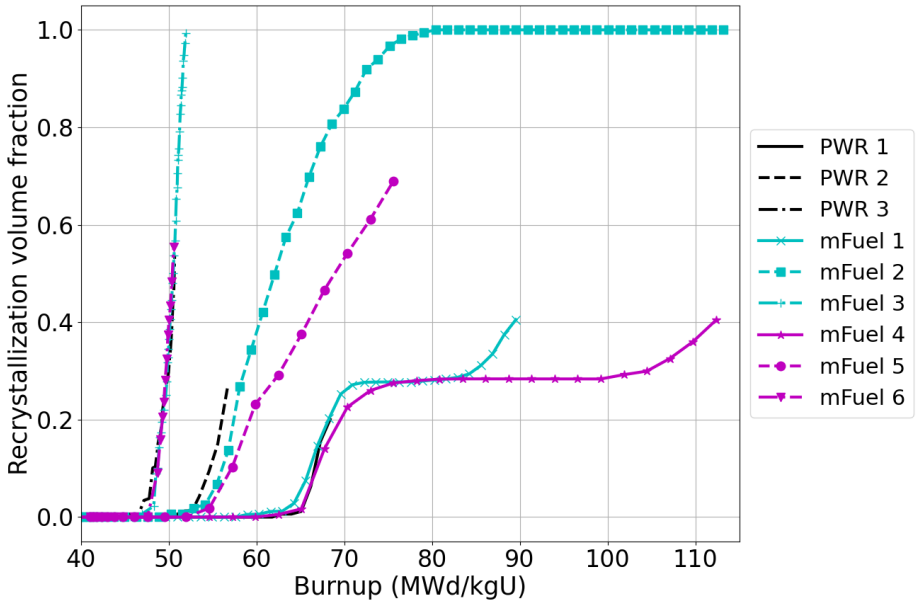

Figure 5. Plots of the recrystallization volume fraction as a function of burnup for PWR fuel cases 1–3 and MiniFuel (mFuel) cases 1–6.

limitation in the discrete nucleation direct modification of order parameters, which should be addressed in future work. The grain boundary mobility is highly temperature-dependent (Arrhenius equation). Therefore, grain boundaries move faster at 950°C, which incorporates new nuclei in a shorter time. Because the nuclei are slowly incorporated into the polycrystalline structure at lower temperatures, the grain boundaries do not form immediately. Thus, nucleation at the boundaries of new grains is not activated until a few time steps after nucleation at the boundaries of pre-existing grains. This effect most likely explains the plateau in the recrystallization fraction observed for the 650°C cases. It could also explain the differences observed between the three cases at the same temperature because of the free energy changes between these cases, which also change the number of nuclei generated at a single time step. Overall, the issue of the delayed nucleation at the boundaries of new grains could be mitigated by tracking new nuclei and temporarily imposing an enhanced grain boundary mobility to new grains until they are properly incorporated into the polycrystalline structure. Moreover, the longer new nuclei take to integrate the polycrystalline system, the more memory is used as a result of mesh refinement. This caused some simulations to end earlier because they exceeded the allocated memory resources.

In comparison with postirradiation characterization data [6], the simulation results show significant differences with respect to the recrystallization amplitudes and rates. In reality, the subdivided grain structure is mostly observed toward the fuel periphery (lower temperature) and expands toward the fuel center (higher temperature) at high burnup, which contradicts the model results' trends. This mismatch between the simulation results and the characterization data is nevertheless expected as a result of the assumption of a fully dense structure, which is not necessarily representative of a real UO_2 microstructure at 40 MWd/kgU, especially at higher temperatures (far from the peripheral region of the pellet). Fission

gas diffusion increases at higher temperatures, which enables bubble formation and growth and reduces the total free energy of the material. In this case, the nucleation probability decreases, and recrystallization occurs significantly later, if at all, compared to the results in Figure 5. For this reason, it is essential to include fission gas bubbles according to the estimated fuel porosity by BISON, either by allowing bubble nucleation or initializing the simulation domain with a number of bubbles included, as done in Figure 2b. The effect of fission gas bubbles on the microstructure evolution is studied in Section 2.2.2.

2.2.2 Porous Microstructure

The ultimate objective of this work was to provide a comparison between the performance of MiniFuel to that of commercial PWR fuel at high burnup and at the microstructural level. To obtain realistic simulation conditions in MARMOT, BISON's predictions were used at the engineering scale, which predicted different porosity levels among the nine simulated cases. Therefore, the total bubble area did not start at the same value, and the material's initial free energy also varied among the studied cases. The temperatures considered in this study do not cause significant diffusion of fission gas atoms and uranium vacancies, and the bubble phase mobility increases with temperature in an Arrhenius relationship. Consequently, the maximum time step allowing numerical convergence was significantly shorter compared to that of the previous simulations (of fully dense structures), especially for higher temperatures. Additionally, the diffusivity of uranium vacancies [34] can be significantly higher than that of fission gas atoms [14], which also shortens the time step. Because of this limitation, the total free energy of the simulated domain for each considered temperature was plotted separately as a function of the simulated irradiation time in Figure 6. The fission rate is different in each of the three cases shown at each temperature. Moreover, the irradiation time is different for each temperature case as a result of the limited maximum time step.

At 650°C (Figure 6a), the highest free energy was obtained in MiniFuel case 1 after PWR fuel case 1. Additionally, MiniFuel case 1 showed the highest free energy among all 9 cases. Therefore, at an equivalent linear heat rate of 8.8 kW/m and an irradiation temperature of 650°C, MiniFuel is expected to undergo recrystallization earlier than any other case considered according to this study. At 650°C and 800°C, the free energies in the three cases were not significantly different, whereas at 950°C (Figure 6c), the total free energy in PWR case 3 is higher than that of the MiniFuel cases; this difference in total free energy could result in a remarkable difference in microstructural features. This result indicates that recrystallization may occur earlier in PWR case 3 compared to MiniFuel cases 3 and 6.

Figure 7 shows the total bubble as a function of irradiation time at each considered temperature. The initial porosity varied among all nine cases, and the total bubble area partially included the smooth interfaces. The simulations show that bubble growth increased with temperature (as expected) as a result of higher diffusivity of both species in the model. The growth rate appears to be similar between the three cases at both 650°C and 800°C, whereas PWR case 3 shows a higher growth rate from MiniFuel cases 3 and 6 at 950°C.

Overall, the free energy decreased at higher temperature, which in theory reduced the nucleation probability. This matches the Electron Backscatter Diffraction characterization results obtained by Gerczak et al. [6], which showed a decrease in restructuring from the fuel pellet periphery to near the midradial region. Nevertheless, beyond the midradial region, restructuring was observed, although to a lesser extent than at the pellet periphery. From the model in this study's perspective, at higher temperature regions, the nucleation probability could be significant if the temperature dependence of the nucleation rate overcomes

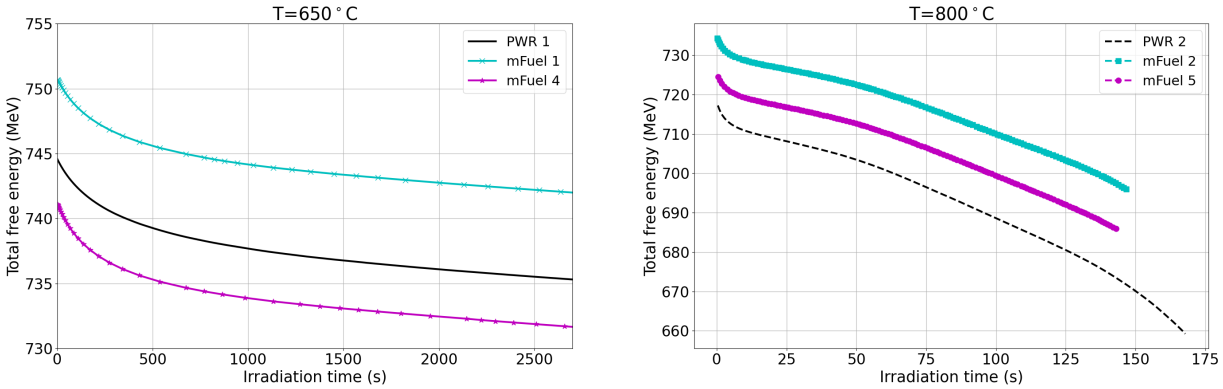

(a)

(b)

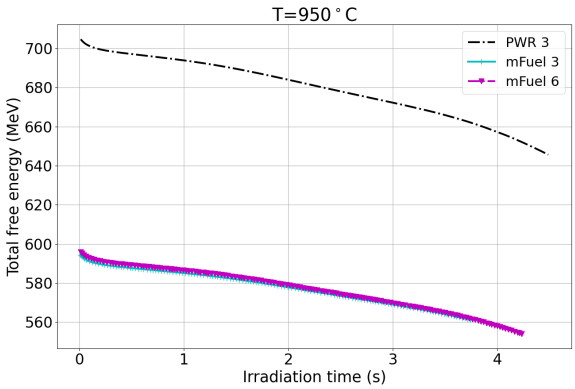

(c)

Figure 6. Plots of the total free energy in the simulated domain as a function of irradiation time at (a) 650°C, (b) 800°C, and (c) 950°C.

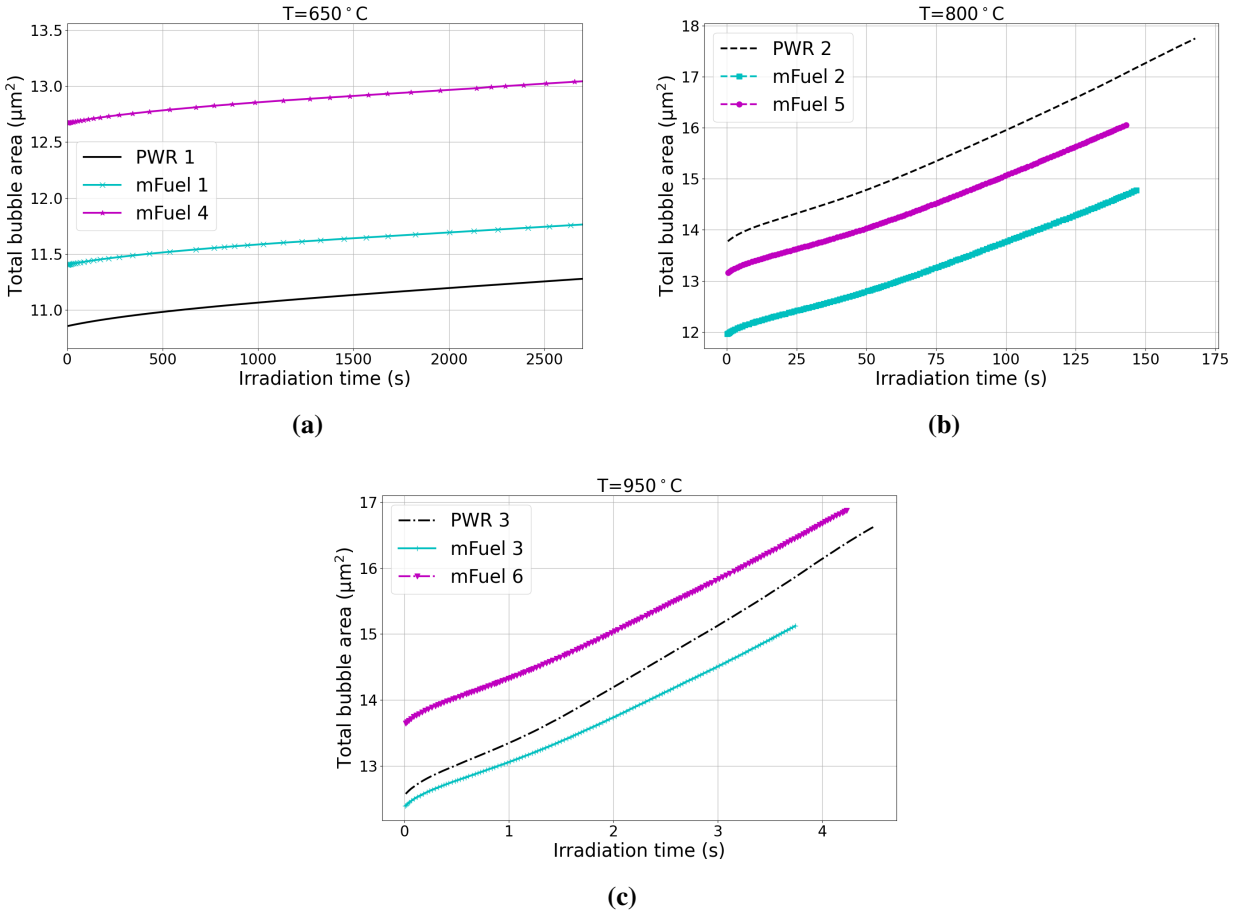

Figure 7. Plots of the total bubble area in the simulated domain as a function of irradiation time at (a) 650°C, (b) 800°C, and (c) 950°C.

the free energy reduction owing to diffusion of uranium vacancies and fission gas atoms to bubbles and temperature-activated grain growth, which decreases the nucleation driving force. Based on the results of the two sets of microstructure evolution simulations showing the competing effects between the temperature-dependent nucleation rate and the free energy reduction by diffusion, higher-temperature simulations might show restructuring in the center of the fuel pellet. Therefore, validation data are being actively pursued to support this theory based on the modeling results. The current model, however, requires further development to address limitations and improve the numerical convergence to determine the restructuring level for each studied case, especially for radial positions between the midradial and central regions. Uncertainties in model parameters such as chemical mobilities, grain boundary properties, and diffusion coefficients affect the quantitative predictions of this model.

2.2.3 Future Work

A physics-based model is needed to provide insight into microstructural changes with radiation dose. Ideally, a restructuring model would include bubble nucleation to allow for a full simulation starting from earlier irradiation cycles without the need for preliminary engineering-scale fuel performance simulations. A more complete model would also account for the formation of intragranular fission gas bubbles and voids as well as the formation and diffusion of uranium interstitials. The contribution of intragranular bubbles and their effect on the gas atoms concentration at grain boundaries can be included through coupling MARMOT to the cluster dynamics code Xolotl, as done in Kim et al. [29]. The inclusion of uranium interstitials along with uranium vacancies can benefit from coupling MARMOT with a binary collision Monte Carlo code such as the MOOSE-based application Magpie, which calculates the production rate of vacancy or interstitial atoms in an irradiated material. In this work, the production rate of uranium vacancy is assumed to be 3× higher than that of gas atoms at all the temperatures considered. However, this does not account for interstitial–vacancy recombination and absorption of vacancies at sinks. Additionally, a mechanistic model of dislocation accumulation is preferable to the empirical relationship to burnup used in this work. This would avoid assuming a uniform dislocation density distribution, which affects the recrystallized grain sizes [18]. Moreover, the time step size must improve to allow for a longer simulation spanning a range of fuel burnups. This longer simulation might benefit from separating the solve for the uranium vacancy chemical potential from other problem variables in a coupled scheme because it has the highest diffusion coefficient. Such coupling could be performed using the MOOSE MultiApp system [42]. Finally, validation of the model is necessary as more characterization data of high burnup UO_2 become available.

3. ACCELERATED MINIFUEL IRRADIATION FLUX DEPRESSION CHARACTERIZATION

AFQ is a process whereby new fuels can be qualified along an accelerated timeline compared to traditional methods. This process is accomplished by using HFIR to provide higher burnups in a shorter time frame than a typical LWR. In theory, fuel specimens irradiated in HFIR are intended to operate within temperature conditions expected in commercial LWR or advanced reactor fuels. However, although temperatures of HFIR-irradiated specimens and LWR fuel are comparable, two items may need to be considered before comparing between the two fuels:

- the effects of self-shielding on the temperature and burnup profiles across a fuel specimen
- the speciation of isotopes in the fuel specimen and their dependence on enrichment

In this analysis, a typical MiniFuel calculation was adapted to consider these items. The input for this calculation is based on an early analysis for the experiment described in [43]. This model considers the support structures of the MiniFuel subcapsule as well as specimens above and below the subcapsule. The fuel specimen in the subcapsule of interest was divided into meshes, which were then evaluated using the HFIR Controller (HFIRCON) code. HFIRCON was developed to automate the workflow for evaluating targets and fuel while they are irradiated in HFIR. This code includes the LAVA Model Interrogator, the Automated Variance Reduction Generator, the ORNL Transformative Neutronics patch for Monte Carlo N-Particle 5 (MCNP5) v1.60, and the Oak Ridge Isotope generation software. This methodology is further described in the following section.

3.1 MATERIALS AND METHODS

The geometry of the fuel specimen, supporting structures, and the subcapsules and assemblies around the supporting structures were based on an early version of the calculation found in [43]. The only changes made to this geometry were to one of the fuel specimens located just above (~0.6 cm) the core centerline in the subassembly location radially closest to the core. This configuration is shown in Figure 8.

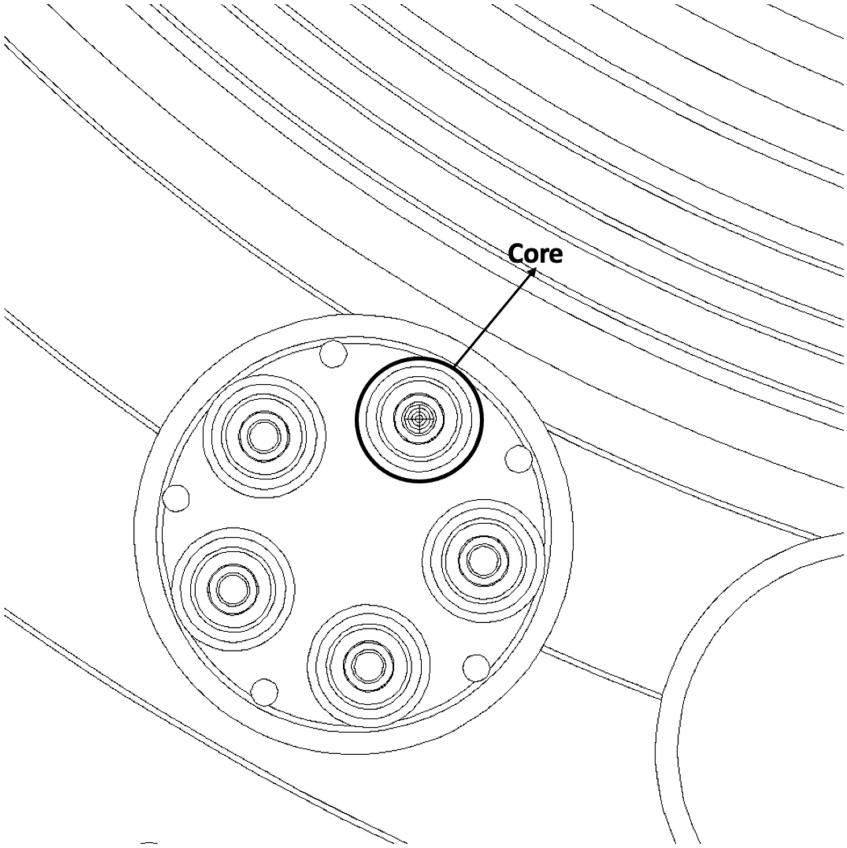

Figure 8. Experimental Assembly from [1] showing the location of the fuel disk used for the self-shielding analysis relative to the core.

Two separate calculations were performed, in which the fuel specimen was divided into volumetric meshes. The first mesh consisted of 17 radial sections with 0.01 cm thickness and 4 axial sections with approximately 0.01 cm thickness for each section. There was a total of 68 voxels in this mesh. The second mesh considered a reduced number of radial and axial sections, considering only four radial and three axial, but this mesh also considered four azimuthal sections in addition to the radial and axial divisions. The additional sections resulted in a mesh with 48 voxels with a thickness of 0.04 cm for the radial section and approximately 0.013 cm for the axial sections, as well as 45° sections for the azimuthal. Figure 9 and Figure 10 show the first mesh (4A17R) and second mesh (3A4R4Q).

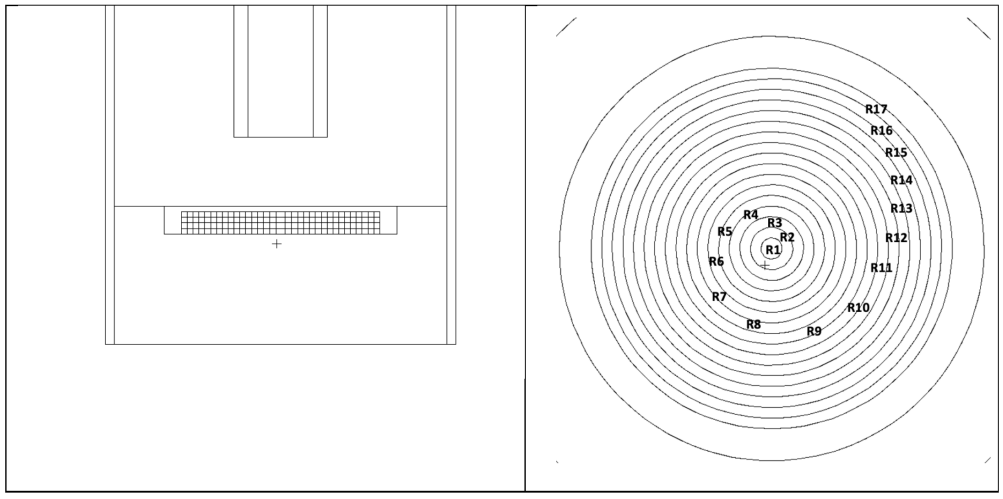

Figure 9. Geometry of mesh 4A17R shown in (*left*) YZ and (*right*) XY plots with radial regions identified in bold. Axial regions go in ascending order from top to bottom.

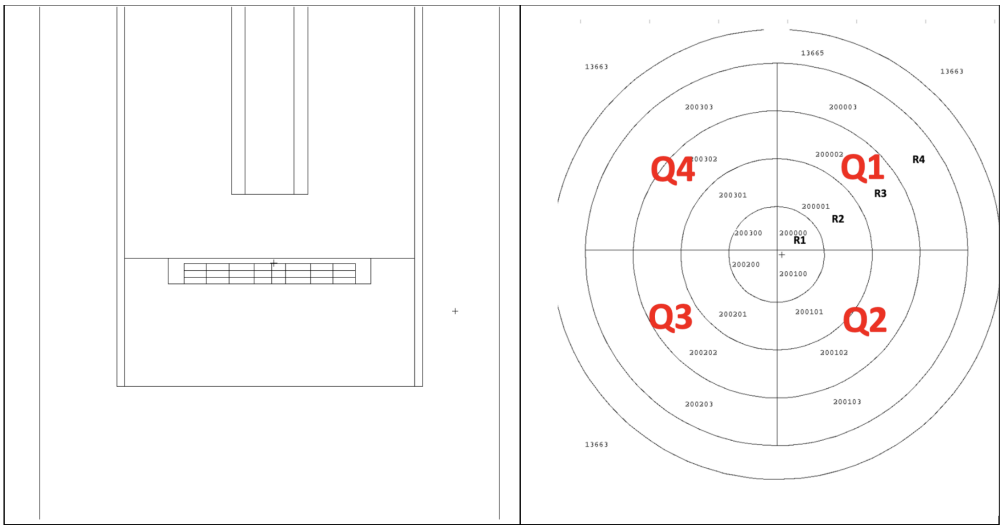

Figure 10. Geometry of mesh 3A4R4Q shown in (*left*) YZ and (*right*) XY plots with radial regions identified in bold black and quadrants identified in bold red. Axial regions go in ascending order from top to bottom.

Both meshes were evaluated for a cycle length of approximately 26 days using control element positions typical of HFIR operation. The controller, in which the parameters of the HFIRCON calculation are described, is included in the Appendix for 4A17R and 3A4R4Q.

3.2 RESULTS

The results of this analysis are considered for the 4A17R and 3A4R4Q meshes separately. One interesting piece of information that can be gained from this comparison is whether having azimuthal sections influences the reported burnup and heating gradients because MCNP averages over an entire voxel in reporting its results. Likewise, because the radial layers of the 3A4R4Q mesh are thicker, information on how influential the layer thickness is can also be gained.

3.2.1 Heating Gradients

For the evaluation of a heating gradient in the specimen, each mesh was evaluated for prompt neutrons, prompt gamma rays, end-of-cycle decay gamma rays, and heating from activation products. All of these heating contributions are output directly from HFIRCON as simple text files. Because HFIRCON produces values for every time step of the calculation, only the maximum values were considered for simplicity.

3.2.1.1 Natural Uranium Specimens

The heating gradient for the 4A17R case is shown in Figure 11 for a single cycle of the natural uranium case. The maximum heating across all time steps was taken for each mesh element as representative. These values were divided by the minimum heating in the mesh to get a factor of change (the lowest of which is 1), which is what is shown in the figures. As expected, the highest heatings occurred at the axial extremes of the fuel specimen and the outer radial ring. The largest factor of difference occurs between the outermost radial ring at 0.17 cm (R17) and the radial ring at 0.16 cm (R16), suggesting that most of the self-shielding is occurring on the outermost part of the fuel disk. The difference in heating as a result of axial variation shows that the upper and lower mesh elements, 1 and 4, have the highest heating, while elements 2 and 3 have the lowest. The largest factor of difference is approximately 1.6× the minimum value for radial element 17 at axial layers 1 and 4.

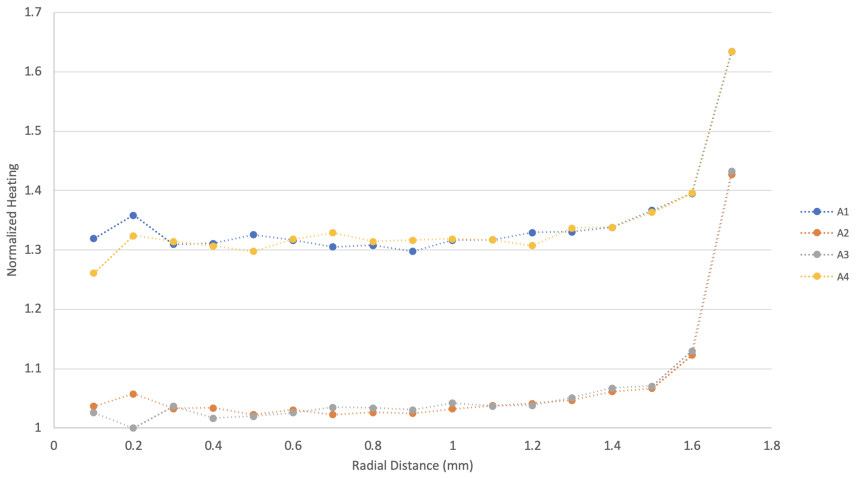

Figure 11. Cycle 1 normalized heating for natural uranium and mesh 4A17R is shown as a function of radial distance for axial locations A1, A2, A3, and A4.

For the second cycle of 4A17R, the heating gradient behaves nearly identical to the first cycle, with the top and bottom axial layers leading the heating factors. And, like the first cycle, the highest heating ratio occurs for radial layer R17. The factor of difference between the minimum value and R17 climbed to approximately 1.7 for the second cycle.

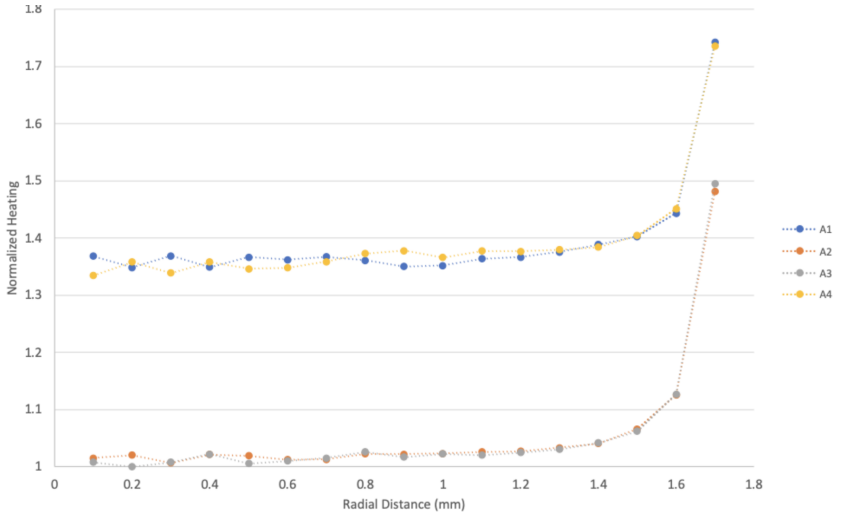

Figure 12. Cycle 2 normalized heating for natural uranium and mesh 4A17R shown as a function of radial distance for axial locations A1, A2, A3, and A4.

For the 3A4R4Q case, the first thing considered was the effect of dividing the fuel disk azimuthally on the heating and burnup. The results of this comparison are shown in Figure 13. The highest heating values are shown in Q1, which is the section facing the core centerline, followed by Q2 and Q4, which flank each side of Q1. The lowest heating is found in Q3, which is the furthest from the core. The largest difference between these values is on the order of approximately 30 W/g between Q1 and Q3.

Because Q1 showed the highest heating of the quadrants, only Q1 was considered for the analysis of the radial and axial gradients in the fuel specimen. Figure 14 shows the heating factor of 3A4R4Q as a function of the radial location of each mesh layer. Like the 4A17R mesh, the heating shows a fairly large factor of increase between the outermost radial layer and next inner layer. However, the heating factor between the two, and overall, is lower than in the 4A17R mesh. Although the inclusion of the azimuthal sections in the fuel mesh does result in a better representation of the heating distribution, it is possible that the thicker radial layers counteract this advantage. As previously mentioned, MCNP averages over an entire cell for its results. Because less radial layers are present in the 3A4R4Q mesh, some of the radial gradient is lost, and the average of the outermost layer is lower. This lower average implies that care should be taken to add more radial layers on the outer part of the fuel specimen in addition to azimuthal sections to fully capture the heating gradients within.

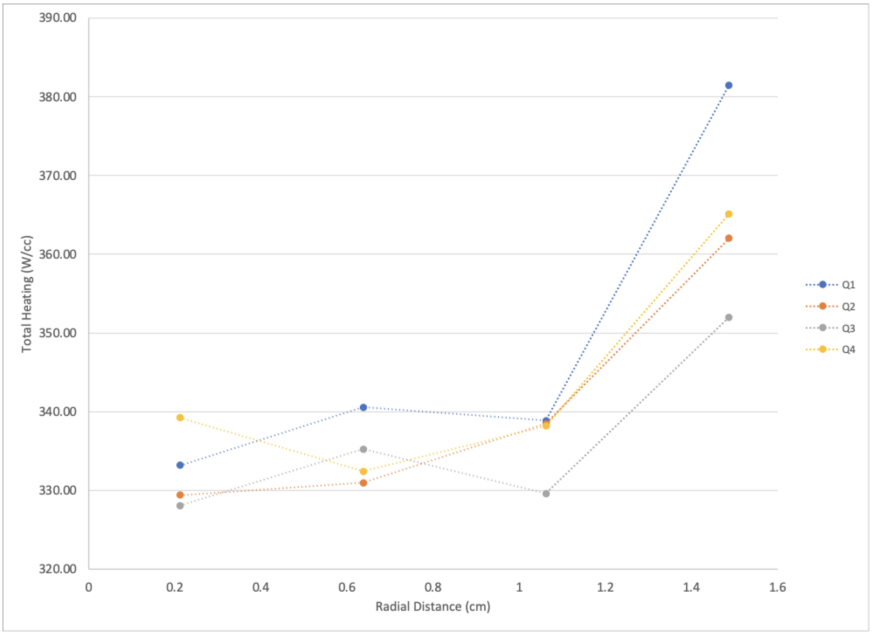

Figure 13. Total heating for the 3A4R4Q mesh as a function of radial distance from the center of the fuel disk. This is shown for azimuthal quadrants Q1, Q2, Q3, and Q4.

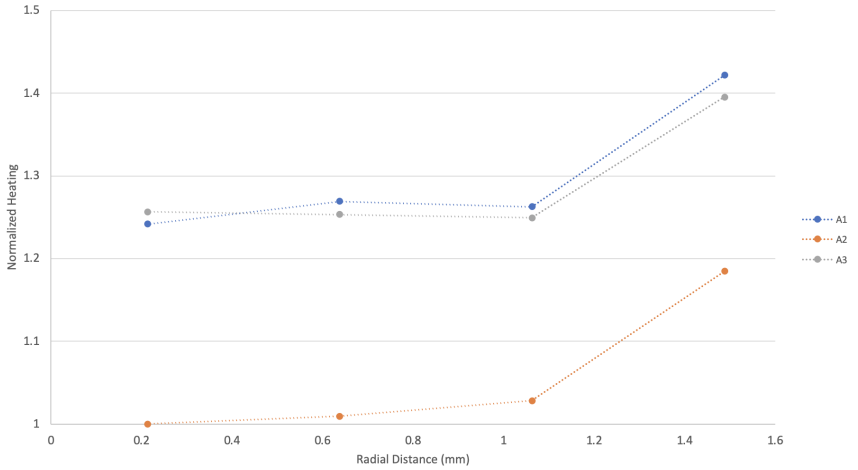

Figure 14. Cycle 1 normalized heating for mesh 3A4R4Q for natural uranium is shown as a function of radial distance for axial locations A1, A2, A3, and A4.

For the second cycle of 3A4R4Q, shown in Figure 15, similar behavior is seen as in the first cycle—increasing heating as the outer radial ring of the mesh is approached. Like the first cycle and the results from the 4A17R mesh, the upper and lower axial layers offer the highest factor of heating.

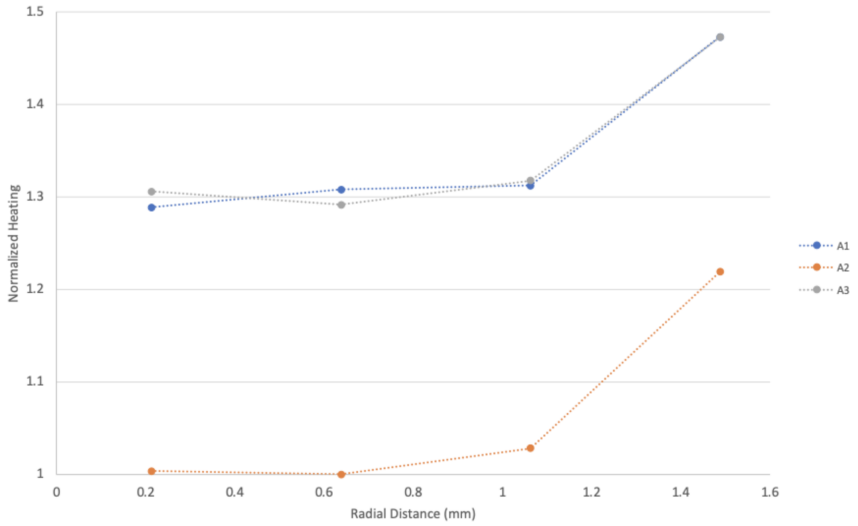

Figure 15. Cycle 2 normalized heating for mesh 3A4R4Q for natural uranium is shown as a function of radial distance for axial locations A1, A2, A3, and A4.

3.2.1.2 6% Enriched Uranium Specimens

For the 6% enriched uranium specimen, only 1 cycle was evaluated for mesh 4A17R because of time constraints as well as based on the results of the first cycle. The difference between the natural and 6% enriched case is stark: although the natural uranium specimen saw a factor of approximately 1.7× difference between the lowest heating element and R17 (the outermost radial region), the 6% enriched uranium case showed a difference of less than 0.05. This difference was true for both the axial and radial variations. The reasoning for this difference could be fairly simple: natural uranium contains a higher concentration of ^{238}U, which parasitically absorbs neutrons during irradiation. Although the amount of ^{238}U was decreased in the specimen (i.e., the enrichment is increased), the self-shielding effect was diminished.

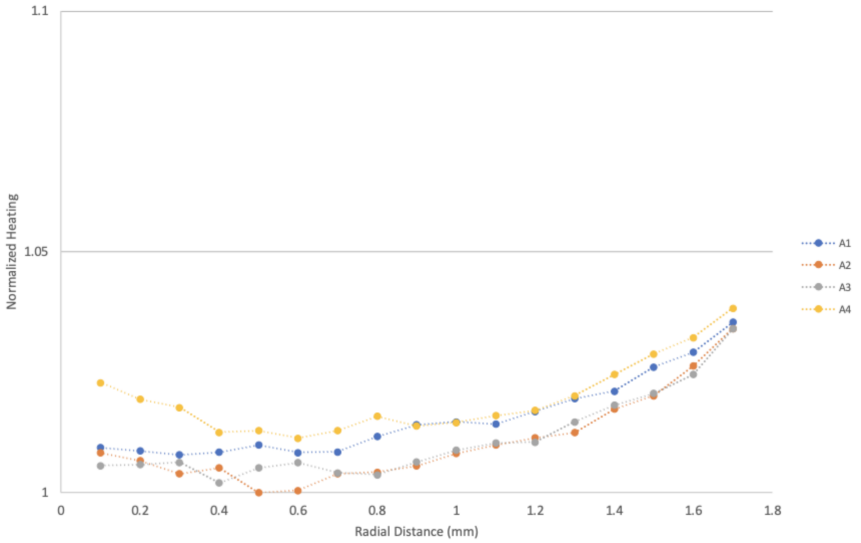

Figure 16. Cycle 1 normalized heating for mesh 4A17R at 6% enrichment is shown as a function of radial distance for axial locations A1, A2, A3, and A4.

Two cycles were evaluated for 3A4R4Q. Like the 4A17R mesh, the effect that radial location within the fuel specimen had on the heating was very small compared to the natural uranium case, yielding less than a 1.05× difference. Additionally, much like the 4A17R mesh, the axial location within the fuel had even less of an effect on the overall heating in the specimen.

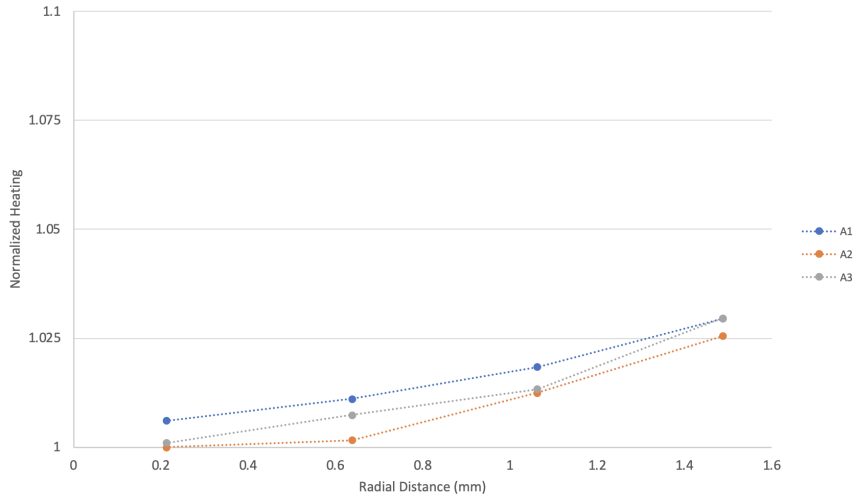

Figure 17. Cycle 1 normalized heating for mesh 3A4R4Q at 6% enrichment is shown as a function of radial distance for axial locations A1, A2, A3, and A4.

For the second cycle of the 6% enriched uranium 3A4R4Q mesh, although the trend of having a lower effect on the heating than the natural uranium case continues, the effect for the second cycle is not as low as during the first cycle. The second cycle shows the highest effect being 1.15× higher than the lowest value

in the mesh. This higher value suggests that the effect to self-shielding for the higher enriched case increases as it is irradiated.

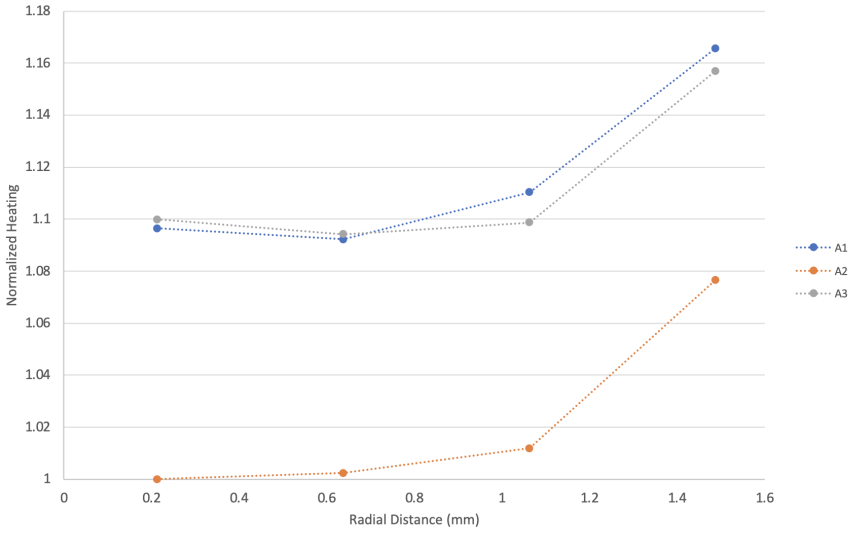

Figure 18. Cycle 2 normalized heating for mesh 3A4R4Q at 6% enrichment is shown as a function of radial distance for axial locations A1, A2, A3, and A4.

3.2.2 Burnup Gradients

For the consideration of the potential effect of self-shielding to the burnup, the fission rates produced by HFIRCON as a simple text file were used to calculate the burnup of the specimen in megawatt days per kilogram of uranium. This calculation was performed using the following equation:

$$BU_t(\frac{\text{MWd}}{\text{kgU}}) = BU_{t-1}(\frac{\text{MWd}}{\text{kgU}}) + \frac{Fission\ Rate_t(\frac{\text{fissions}}{\text{cm}^3\text{s}}) \times 200(\frac{\text{MeV}}{\text{fission}}) \times \Delta t(\text{d}) \times \frac{1.602\times10^{-13}\text{J}}{1\text{MeV}} \times \frac{1\text{Ws}}{1\text{J}} \times \frac{1\text{MW}}{10^6\text{W}}}{\rho(\frac{\text{g}}{\text{cm}^3}) \times fU \times (\frac{1\text{kg}}{10^3\text{g}})}$$

where BU_t is the burnup at time step t, BU_{t-1} is the burnup at time step $t-1$, Δt is the change in time between time step t and time step $t-1$, ρ is the density of the specimen, and fU is the fraction of uranium in the specimen. Here, ρ is taken to be 10.43 g/cm^3, and fU is 0.88. The density and fraction of uranium are based on the specific specimen.

3.2.2.1 Natural Uranium Specimens

The burnup gradient for the 4A17R case is shown in Figure 19 for a single cycle of the natural uranium case. The burnup at the end of the cycle, which is the maximum value, was considered as representative. As expected, the highest burnup occurred at the axial extremes of the fuel specimen and the outer radial ring. The largest factor of difference occurred between the outermost radial ring at 0.17 cm (R17), and the radial ring at 0.16 cm (R16), suggesting that most of the self-shielding occurred on the outermost part of the fuel disk. The difference in burnup as a result of axial variation shows that the upper and lower mesh

elements, 1 and 4, had the highest heating, and elements 2 and 3 had the lowest. The largest factor of difference is approximately 1.4× the minimum value for radial element 17 at axial layers 1 and 4.

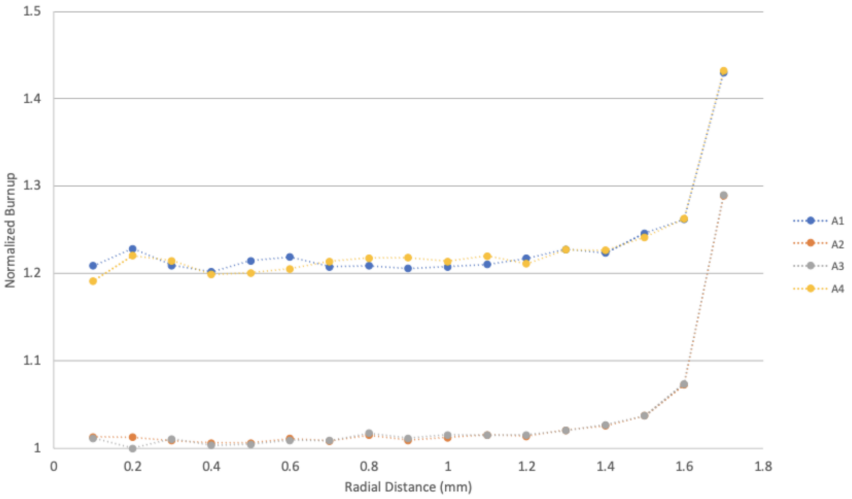

Figure 19. Cycle 1 normalized burnup for natural uranium and mesh 4A17R is shown as a function of radial distance for axial locations A1, A2, A3, and A4.

Figure 20 shows the impact to burnup on the 4A17R mesh as a function of radial distance for the second cycle. Like the first cycle, the highest factor of difference in the mesh is seen at the outer radial location of the specimen. This effect increases as the specimen is irradiated for a second cycle. The highest factor of difference during the second cycle for the 4A17R mesh was ~1.6.

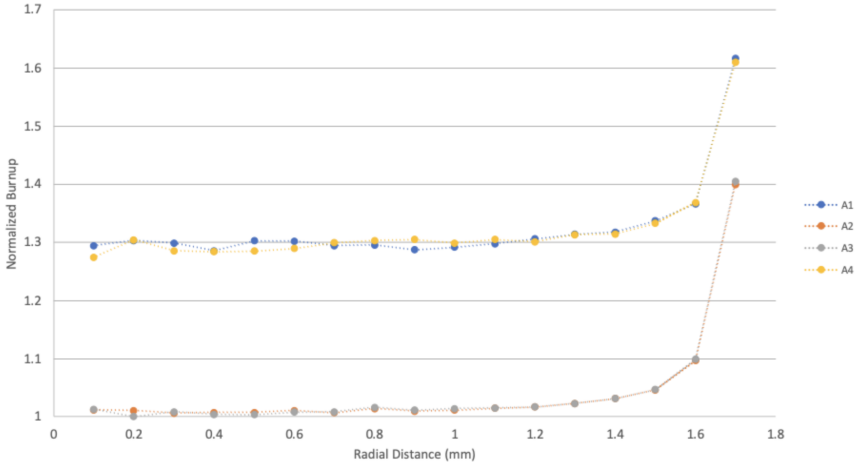

Figure 20. Cycle 2 normalized burnup for natural uranium and mesh 4A17R is shown as a function of radial distance for axial locations A1, A2, A3, and A4.

For the 3A4R4Q mesh, 21 shows the normalized burnup as a function of radial distance. The overall impact of the radial and axial location of the mesh elements is less than what is seen for the 4A17R mesh.

This is likely a result of using a coarser radial mesh than in the 4A17R case, and the higher values being averaged with values from lower-heating areas within the larger mesh voxels of the 3A4R4Q mesh. The highest impact to burnup for the first cycle of the 3A4R4Q mesh is approximately 1.3.

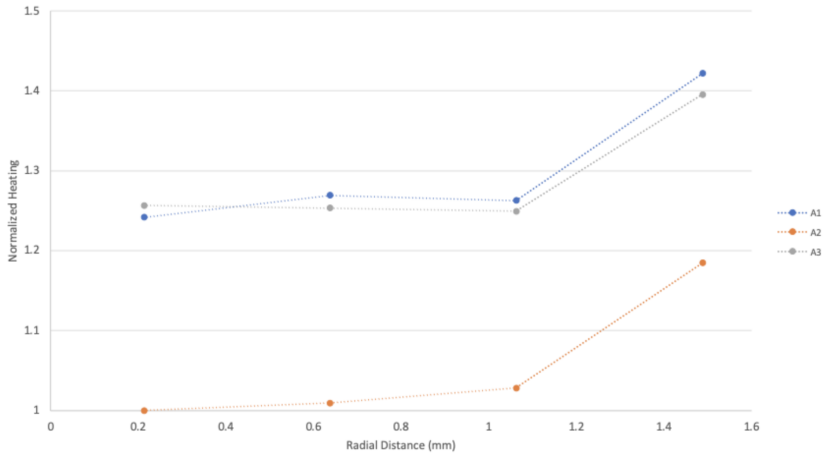

Figure 21. Cycle 1 normalized burnup for mesh 3A4R4Q for natural uranium is shown as a function of radial distance for axial locations A1, A2, A3, and A4.

The second cycle of 3A4R4Q mesh for natural uranium is shown in Figure 22. Consistent with the 4A17R mesh, the impact to radial and axial location increases as the irradiation is continued in the second cycle. The highest factor of increase in the burnup is approximately 1.5.

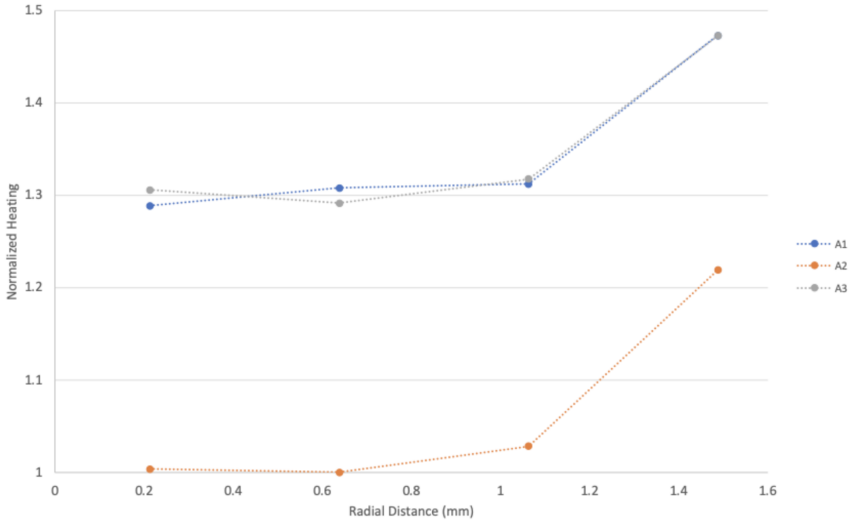

Figure 22. Cycle 2 normalized burnup for mesh 3A4R4Q for natural uranium is shown as a function of radial distance for axial locations A1, A2, A3, and A4.

3.2.2.2 6% Enriched Uranium Specimen

For the 6% enriched specimen, only 1 cycle was evaluated for mesh 4A17R. This was both due to time constraints as well as based on the results of the first cycle. While the natural uranium specimen saw a factor of approximately 1.4 difference between the lowest burnup and R17 burnup, the outermost radial region, the 6% enriched case shows a difference of approximately 1.1. This reduced impact is the case for both the axial and radial variations.

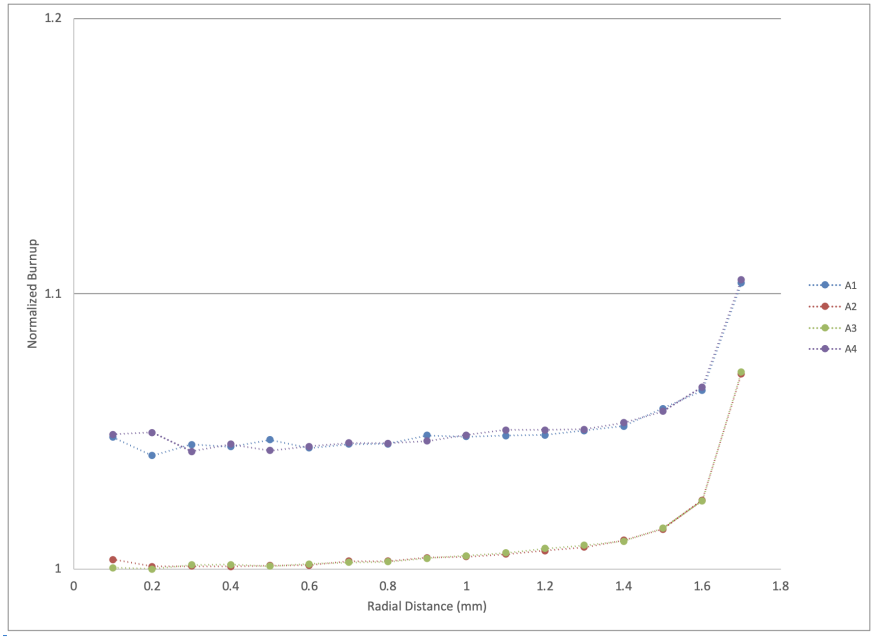

Figure 23. Cycle 1 normalized burnup for mesh 4A17R at 6% enrichment is shown as a function of radial distance for axial locations A1, A2, A3, and A4.

Figure 24 shows the burnup gradient for the 3A4R4Q mesh at 6% enrichment. Like the natural uranium case, the 3A4R4Q mesh appears to underestimate the burnup as a result of the coarser mesh being considered in the problem. The highest factor of difference in this mesh was approximately 1.075.

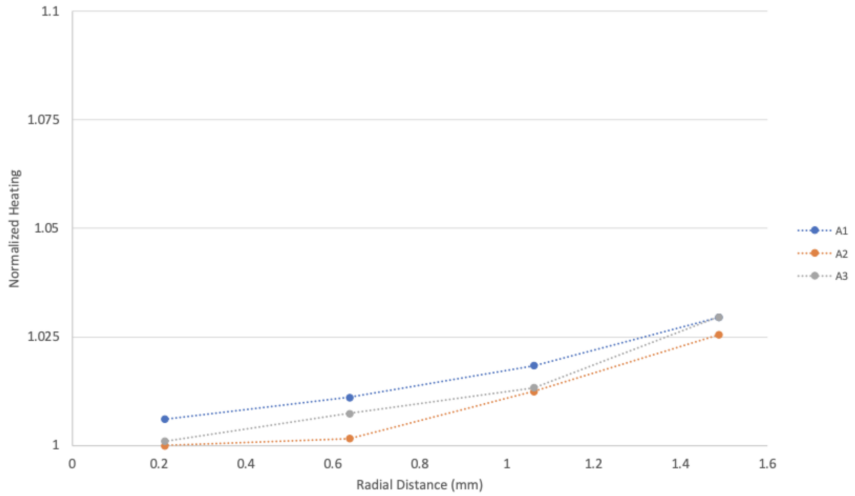

Figure 24. Cycle 1 normalized burnup for mesh 3A4R4Q at 6% enrichment is shown as a function of radial distance for axial locations A1, A2, A3, and A4.

The second cycle of the 3A4R4Q mesh at 6% enrichment shows the same relationship between the first and second cycle as the natural case, which is a noticeable increase relative to the first cycle-though this impact is significantly more pronounced for the natural uranium case than the 6% enrichment. The maximum factor of difference here is approximately 1.15.

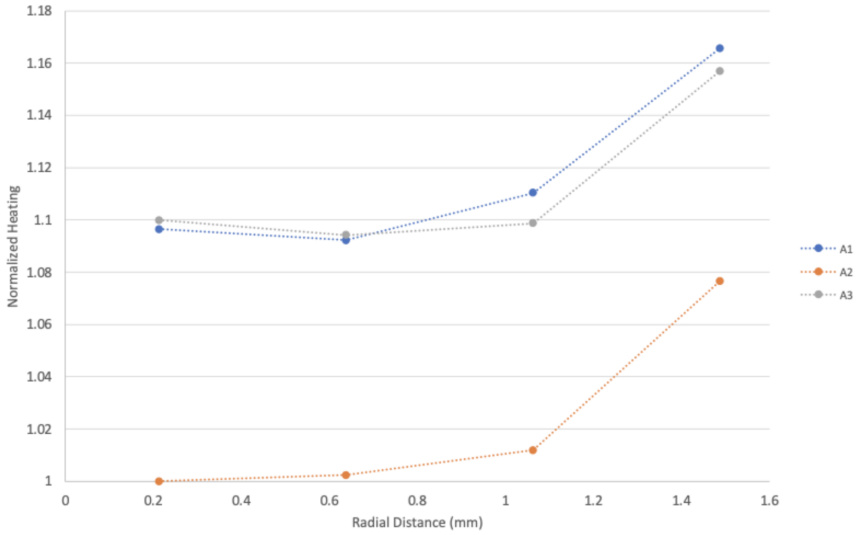

Figure 25. Cycle 2 normalized burnup for mesh 3A4R4Q at 6% enrichment is shown as a function of radial distance for axial locations A1, A2, A3, and A4.

3.2.3 Fission Product Inventories

In addition to the heating and burnup gradients, the speciation of important isotopes in the fuel were also considered as a function of radial and axial distance from the center of the fuel specimen. HFIRCON produces HDF5 files associated with the calculation that contains information about properties such as flux, relative uncertainty, and isotopic inventories. The isotopic inventories contain information about every isotope considered in the problem and the masses of these isotopes in each cell considered. For each mesh and enrichment, the isotopic inventories were considered for the last time step of the cycle for simplicity. Only the radial locations were considered in this study because the effect of radial location was greater than the axial location for the heating and burnup gradients. Additionally, only the first cycle results are shown because the change between the first and second cycles was minimal.

3.2.3.1 Natural Uranium Specimens

For the natural uranium 4A17R mesh, Figure 26 shows the masses of ^{235}U, ^{238}U, ^{239}Pu, ^{240}Pu, and ^{241}Pu as a function of radial location, all of which are normalized to the minimum mass of each isotope in the mesh at the topmost outer axial location. Although the ^{235}U and ^{238}U masses changed very little relative to their location in the specimen, the masses of ^{239}Pu, ^{240}Pu, and ^{241}Pu increased as one approached the outer radial layer of the fuel specimen. This increase is logical: if the lower heating and burnup seen in the center of the fuel specimen is because of the parasitic absorption of neutrons by ^{238}U, then the specimen will produce a larger quantity of the plutonium isotopes in the location in which most of the absorption occurs. Because the ^{238}U absorbed neutrons on the outer layer of the fuel pellet, these neutrons were unable to penetrate further into the fuel specimen to either fission the ^{235}U or be absorbed by ^{238}U. The highest factor of increase was ~1.35 between the lowest and highest masses in the mesh.

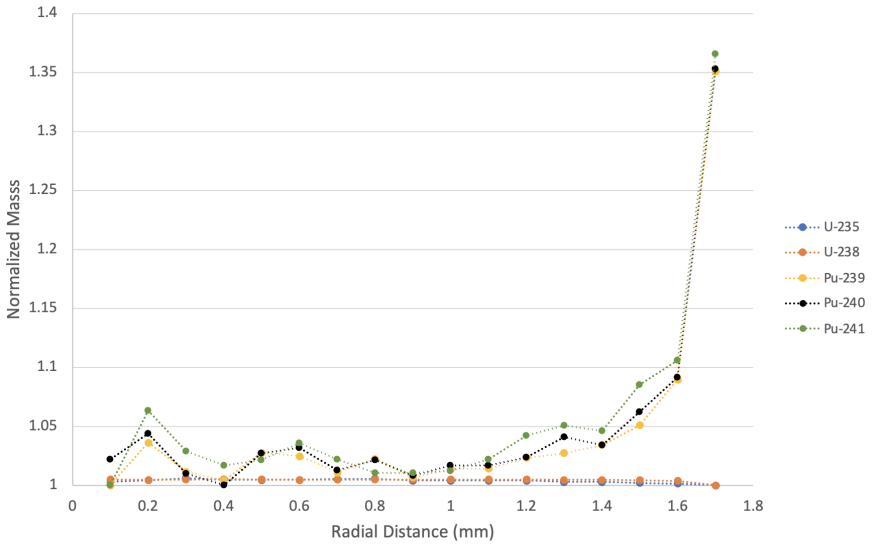

Figure 26. Cycle 1 normalized mass for isotopes ^{235}U, ^{238}U, ^{239}Pu, ^{240}Pu, and ^{241}Pu for the 4A17R mesh for natural uranium.

The 3A4R4Q mesh shows similar behavior in Figure 27, where the plutonium isotopes have a higher mass concentration in the outer layer of the fuel specimen. Like the heating and burnup results, the lower factor of mass increase relative to the 4A17R mesh is probably because of the 3A4R4Q mesh being too coarse to capture some of the differences within the outer radial mesh layer. The highest factor of increase for this mesh was ~1.2.

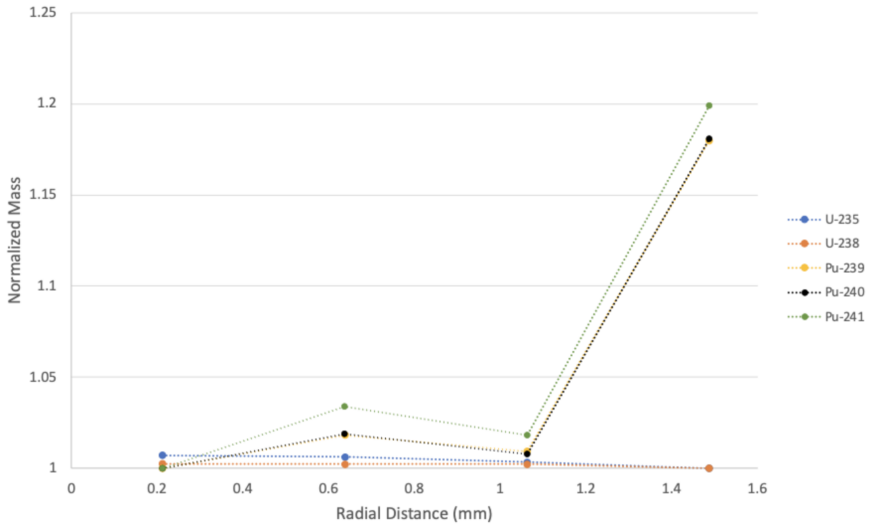

Figure 27. Cycle 1 normalized mass for isotopes ^{235}U, ^{238}U, ^{239}Pu, ^{240}Pu, and ^{241}Pu for the 3A4R4Q mesh for natural uranium.

3.2.3.2 6% Enriched Uranium Specimens

For the 6% enriched case, the 4A17R mesh showed almost identical behavior as in the natural cases. The presence of ^{238}U primarily affected the outer radial layer, shielding neutrons from penetrating further into the fuel specimen. However, because less ^{238}U was present overall in the 6% enriched specimen, the heating and burnup was affected less than in the natural cases.

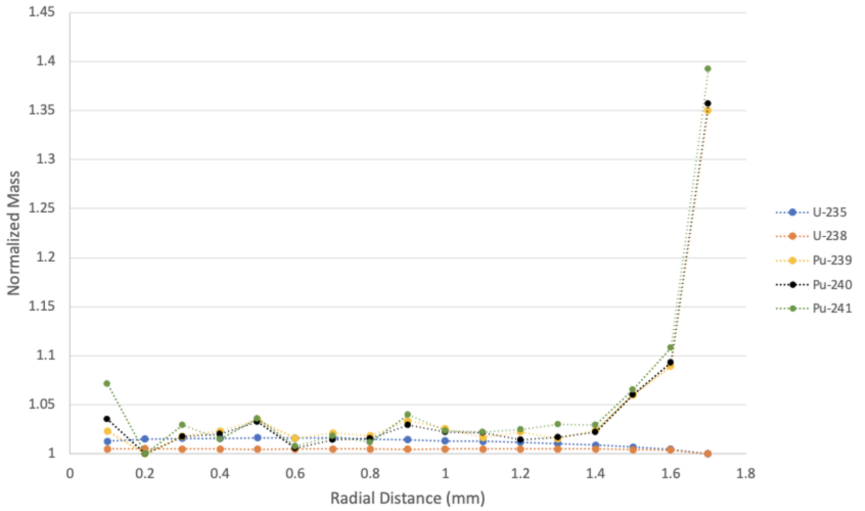

Figure 28. Cycle 1 normalized mass for isotopes ^{235}U, ^{238}U, ^{239}Pu, ^{240}Pu, and ^{241}Pu for the 4A17R mesh at 6% enrichment.

Like the 4A17R case, the behavior of the natural and 6% enrichment is nearly identical, with the highest factor of difference being ~1.2.

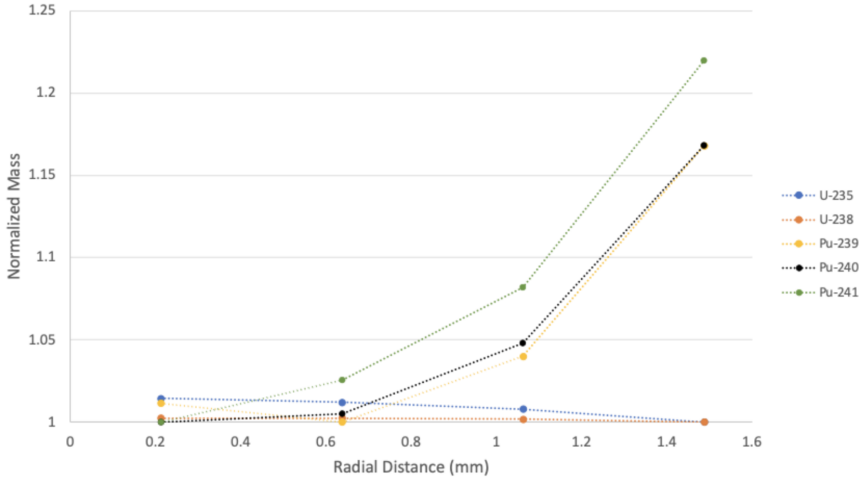

Figure 29. Cycle 1 normalized mass for isotopes ^{235}U, ^{238}U, ^{239}Pu, ^{240}Pu, and ^{241}Pu for the 3A4R4Q mesh at 6% enrichment.

3.3 FISSION PRODUCT SPECIATION IN HIGH-BURNUP FUEL

A primary cause for concern with the AFQ method is that the fuel performance of MiniFuel may not be representative of performance that would occur under prototypic LWR conditions. This concern occurs because the primary fissile material is 95% ^{239}Pu fission in MiniFuel compared to 75% ^{235}U for LWR fuel. Figure 30 shows the fission yield curves for ^{235}U and ^{239}Pu [2]. The general trends are the same, including

that the yield distribution is camelback-shaped with two maxima. For a thermal neutron spectrum below a mass number of approximately 115, the ^{239}Pu fission yield curve shifted towards slightly higher mass numbers. Above mass 115, both ^{235}U and ^{239}Pu curves essentially overlap. This overlap shows that certain fission products (FPs) will be more important (those within the 80–110 range) than others when trying to understand the difference between AFQ fuel and LWR fuel.

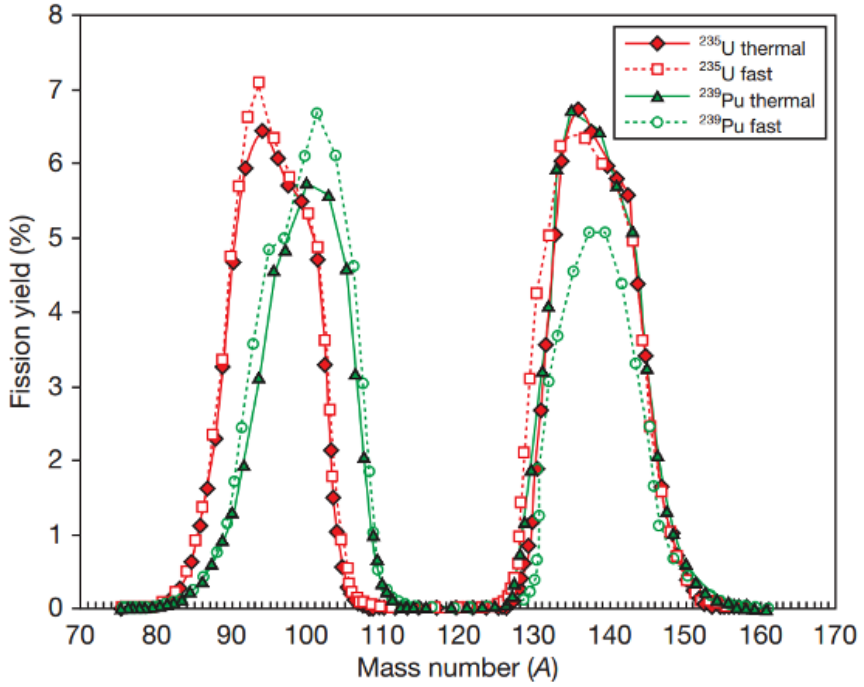

Figure 30. Fast and thermal neutron fission product yield curves for ^{235}U and ^{239}Pu [2].

Acknowledging the reliability of AFQ to provide fuel performance data relevant for LWR conditions cannot be based only on the difference for ^{235}U and ^{239}Pu fission yield; the distribution and nature of each element created in the fuel during reactor operation must also be assessed. Different FPs have very different physical and chemical interactions with the fuel matrix. Some do not react with the fuel, some are found as metallic precipitates, and others react with the fuel matrix to form separate phases. More than 40 elements are produced during fission in a nuclear reactor, and though their concentrations are relatively low compared to the fuel, they can have a significant effect on fuel performance. The chemical state of FPs in oxide fuels are well investigated. Distribution oxide fuels have been grouped into four classes depending on their chemical state in the fuel [2–4, 44–48].

- Group I, the volatile and gaseous fission products—He, Kr, Xe, Br, Rb, Cs, Te, and I
- Group II, metallic precipitates (white phase)—Mo, Tc, Ru, Rh, Pd, Ag, Cd, In, Sn, Sb, and Te
- Group III, oxide precipitates (gray phase)—Rb, Cs, Sr, Ba, Zr, Nb, Mo, and Te
- Group VI, dissolved as oxides in the fuel matrix—Sr, Ra, Zr, Nb, Y, Te, Cs, Ba, La, Ce, Pr, Nd, Pm, Sm, Eu, and the actinide

Some fission products (e.g., Mo, Cs) can exist in multiple groups or chemical forms. Piro et al. [3] demonstrated how FP generation changed as a function of burnup (Figure 31) and how the rate of accumulate in the fuel varied from one chemical element to another.

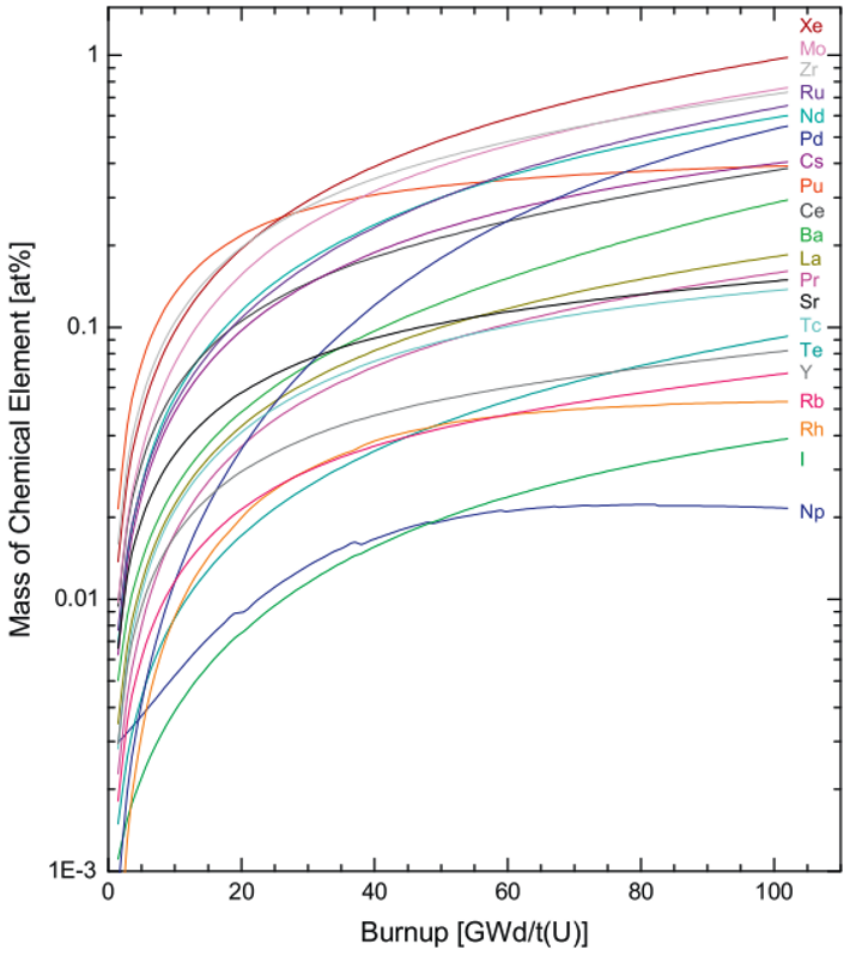

Figure 31. Predicted FP generation as a function of burnup by Piro et al. [3].

Understanding and predicting nuclear fuel behavior in power reactors has been a longstanding problem because of the complexity of the phenomena and the difficulty representing them both separately and in concert. FP phase distribution is dependent on the temperature, burnup, oxygen potential, and the amount of FP element generated [2–4, 44–48]. Thermodynamic computations have been used to predict the equilibrium combination of phases and their composition by determining a unique combination of species and phases that yields the minimum value of the integral Gibbs energy of a closed isothermal–isobaric system subject to mass balance constraints and the Gibbs phase rule [3, 4]. Besmann et al. [4] predicted phase speciation as a function of burnup (Figure 32). The ability to predict the chemical state and elemental potentials in the fuel undergoing accelerated irradiation is important to obtain accurate fuel performance modeling and determine whether the method is valuable for predicting behavior under LWR operations. Future work will use the present study's self-shielding evaluation results to calculate the corresponding FP phase distribution with burnup in MiniFuel.

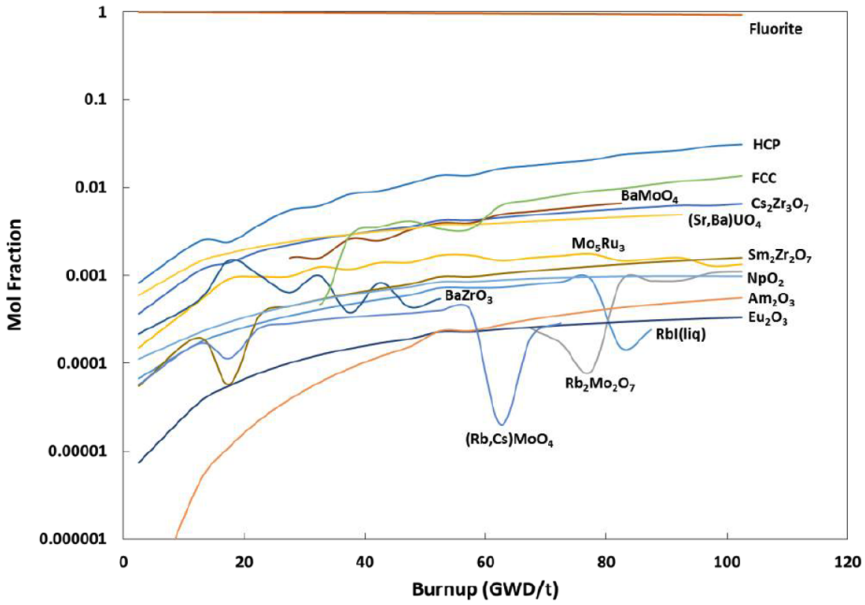

Figure 32. FP phase distribution as a function of burnup predicted by Besmann et al. [4].

4. CONCLUSION

In this work, a phase–field model of UO_2 fuel microstructural evolution that includes nucleation of new grains at high radiation dose was developed using the MARMOT finite element–based code. The initial conditions of the simulations used irradiation conditions and microstructural features predicted by engineering-scale calculations performed in BISON for PWR fuel as well as MiniFuel specimens assuming approximated HFIR conditions (VXF positions). Two sets of nine cases were performed with varying temperatures and fission rates. The first set did not include fission gas bubbles and had three grains initially. The CNT-based nucleation model predicted earlier onset of restructuring at higher temperatures regardless of the fission rate considered. Then, when bubbles were added in the initial setup of a second set of simulations, the model predicted that the system with the highest free energy was the MiniFuel microstructure irradiated with an equivalent linear heat rate of 8.8 kW/m and at the lowest temperature considered (650°C). The model also predicted that higher temperature cases resulted in a lower total free energy, which decreased the likelihood of recrystallization compared to other cases. These initial results agree with characterization data near the fuel pellet periphery. The two sets of simulations indicated that the competing effects between the temperature-dependent grain nucleation rate and the free energy reduction by diffusion at higher temperature could result in recrystallization at even higher temperatures than those considered in this study according to the proposed approach. However, the discussed limitations in this approach must be addressed in future work to reach the recrystallization level in the second set of simulations and to perform these simulations at higher temperatures (central fuel pellet region). Overall, the model results were consistent with the simulation setup in both sets. Additionally, future work will use a multiscale approach to improve the accuracy of the concentrations of point defects and fission gas behavior.

This work also addressed the evaluation of self-shielding on a typical MiniFuel specimen. This was done with two different meshes across the fuel disk: a mesh consisting of 17 radial and 4 axial layers and a mesh with 4 radial, 3 axial, and 4 azimuthal layers. Although the inclusion of the azimuthal layers makes a difference to the overall heating seen in each quadrant, this difference is minimal compared to the effect of the radial layer thickness. The outer radial layer for both meshes showed the highest factor of difference within the mesh. Less radial layers resulted in lower factors of difference, suggesting that a finer radial mesh is necessary for the outer layer of the fuel specimen to truly capture the changes throughout. The effect of enrichment on self-shielding shows that the higher the enrichment, the lower the self-shielding owing to a lower amount of ^{238}U. The natural uranium cases showed a larger effect in both heating and burnup results, with the largest difference being seen in the radial and axial extremes of the meshes. The highest factor of difference for the heating was ~1.7 for the natural uranium case and ~1.15 for the 6% enrichment, and the highest factor of difference for the burnup was ~1.6 for the natural uranium case and ~1.15 for the 6% enrichment. For the heating and burnup for both meshes, the difference between the inner and outer radial layers increased with additional irradiation. The speciation within the fuel specimen was also considered as a function of radial distance from the center, and it was found that the outer radial location had the highest concentration of ^{239}Pu, ^{240}Pu, and ^{241}Pu for both the natural uranium and 6% enriched cases, further confirming that the reduced heating and burnup in the center of the fuel specimen is because of parasitic absorption of neutrons from ^{238}U in the fuel. Future work should consider a finer axial mesh on the outer layer of the fuel as well as the implementation of azimuthal layers. Furthermore, the effects of multiple cycles should be explored further to determine the trend of increased discrepancies between the inner and outer layers of the fuel continues and whether the difference in enrichment becomes less important as irradiation continues.

References

[1] Douglas C Crawford, Douglas L Porter, Steven L Hayes, Mitchell K Meyer, David A Petti, and Kemal Pasamehmetoglu. An approach to fuel development and qualification. *Journal of Nuclear Materials*, 371(1-3):232–242, 2007.

[2] D.D. Baron and L. Hallstadius. 2.19 - fuel performance of light water reactors (uranium oxide and mox). In Rudy J.M. Konings, editor, *Comprehensive Nuclear Materials*, pages 481–514. Elsevier, Oxford, 2012.

[3] MHA Piro, J Banfield, Kevin T Clarno, Srdjan Simunovic, Theodore M Besmann, BJ Lewis, and WT Thompson. Coupled thermochemical, isotopic evolution and heat transfer simulations in highly irradiated UO_2 nuclear fuel. *Journal of Nuclear Materials*, 441(1-3):240–251, 2013.

[4] Theodore M. Besmann, Jacob W. McMurray, and Srdjan Simunovic. Application of thermochemical modeling to assessment/evaluation of nuclear fuel behavior. *Calphad*, 55:47–51, 2016. Christopher W. Bale Symposium - Thermodynamic Applications, Optimizations and Simulations in High Temperature Processes.

[5] Kurt A Terrani, Nathan A Capps, Matthew J Kerr, Christina A Back, Andrew T Nelson, Brian D Wirth, Steven L Hayes, and Chris R Stanek. Accelerating nuclear fuel development and qualification: Modeling and simulation integrated with separate-effects testing. *Journal of Nuclear Materials*, 539:152267, 2020.

[6] Tyler J Gerczak, Chad M Parish, Philip D Edmondson, Charles A Baldwin, and Kurt A Terrani. Restructuring in high burnup UO_2 studied using modern electron microscopy. *Journal of Nuclear Materials*, 509:245–259, 2018.

[7] Christian M Petrie, Joseph R Burns, Alicia M Raftery, Andrew T Nelson, and Kurt A Terrani. Separate effects irradiation testing of miniature fuel specimens. *Journal of Nuclear Materials*, 526:151783, 2019.

[8] T Sonoda, M Kinoshita, ILF Ray, T Wiss, H Thiele, D Pellottiero, VV Rondinella, et al. Transmission electron microscopy observation on irradiation-induced microstructural evolution in high burn-up UO_2 disk fuel. *Nuclear Instruments and Methods in Physics Research Section B: Beam Interactions with Materials and Atoms*, 191(1-4):622–628, 2002.

[9] Vincenzo V. Rondinella and Thierry Wiss. The high burn-up structure in nuclear fuel. *Materials Today*, 13(12):24–32, 2010.

[10] K Lassmann, CT Walker, J Van de Laar, and F Lindström. Modelling the high burnup UO_2 structure in lwr fuel. *Journal of nuclear materials*, 226(1-2):1–8, 1995.

[11] J-P Hiernaut, T Wiss, J-Y Colle, H Thiele, CT Walker, W Goll, and RJM Konings. Fission product release and microstructure changes during laboratory annealing of a very high burn-up fuel specimen. *Journal of Nuclear Materials*, 377(2):313–324, 2008.

[12] J Spino, J Cobos-Sabate, and F Rousseau. Room-temperature microindentation behaviour of lwr-fuels, part 1: fuel microhardness. *Journal of nuclear materials*, 322(2-3):204–216, 2003.

[13] Charlyne A Smith, Sudipta Biswas, Brandon D Miller, Boopathy Kombaiah, David Frazer, Dennis D Keiser, and Assel Aitkaliyeva. High burnup structure formation in u-mo fuels. *Journal of Nuclear Materials*, 563:153617, 2022.

[14] JA Turnbull, CA Friskney, JR Findlay, FA Johnson, and AJ Walter. The diffusion coefficients of gaseous and volatile species during the irradiation of uranium dioxide. *Journal of Nuclear Materials*, 107(2-3):168–184, 1982.

[15] W Wu, D Montiel, JE Guyer, PW Voorhees, JA Warren, D Wheeler, L Gránásy, T Pusztai, and OG Heinonen. Phase field benchmark problems for nucleation. *Computational Materials Science*, 193:110371, 2021.

[16] J Rest and GL Hofman. Dynamics of irradiation-induced grain subdivision and swelling in u3si2 and UO_2 fuels. *Journal of Nuclear materials*, 210(1-2):187–202, 1994.

[17] Linyun Liang, Zhi-Gang Mei, and Abdellatif M Yacout. Fission-induced recrystallization effect on intergranular bubble-driven swelling in u-mo fuel. *Computational Materials Science*, 138:16–26, 2017.

[18] M Gomaa Abdoelatef, Fergany Badry, Daniel Schwen, Cody Permann, Yongfeng Zhang, and Karim Ahmed. Mesoscale modeling of high burn-up structure formation and evolution in UO_2. *Jom*, 71(12):4817–4828, 2019.

[19] Matias G Marquez, Abderrafi M Ougouag, and Bojan Petrovic. Model for radiation damage-induced grain subdivision and its influence in u3si2 fuel swelling. *Annals of Nuclear Energy*, 145:105712, 2020.

[20] K Nogita and K Une. Irradiation-induced recrystallization in high burnup UO_2 fuel. *Journal of Nuclear Materials*, 226(3):302–310, 1995.

[21] R.L. Williamson, J.D. Hales, S.R. Novascone, M.R. Tonks, D.R. Gaston, C.J. Permann, D. Andrs, and R.C. Martineau. Multidimensional multiphysics simulation of nuclear fuel behavior. *Journal of Nuclear Materials*, 423(1):149–163, 2012.

[22] Nathan Capps, Aaron Wysocki, Andrew Godfrey, Benjamin Collins, Ryan Sweet, Nicholas Brown, Soon Lee, Nicholas Szewczyk, and Susan Hoxie-Key. Full core loca safety analysis for a pwr containing high burnup fuel. *Nuclear Engineering and Design*, 379:111194, 2021.

[23] Amani Cheniour and Ryan T. Sweet. Sensitivity evaluation of fuel models to determine the impact of dilute additives on integral fuel performance. Technical Report ORNL/SPR-2022/2422, Oak Ridge National Laboratory, Oak Ridge, TN, USA, 2022.

[24] Amani Cheniour, Giovanni Pastore, Jason M Harp, Christian M Petrie, and Nathan A Capps. Application of bison to UO_2 minifuel fission gas release analysis. *Journal of Nuclear Materials*, 565:153686, 2022.

[25] Nele Moelans, Bart Blanpain, and Patrick Wollants. Quantitative analysis of grain boundary properties in a generalized phase field model for grain growth in anisotropic systems. *Physical Review B*, 78(2):024113, 2008.

[26] Srujan Rokkam, Anter El-Azab, Paul Millett, and Dieter Wolf. Phase field modeling of void nucleation and growth in irradiated metals. *Modelling and simulation in materials science and engineering*, 17(6):064002, 2009.

[27] John S Lowengrub, Andreas Rätz, and Axel Voigt. Phase-field modeling of the dynamics of multicomponent vesicles: Spinodal decomposition, coarsening, budding, and fission. *Physical Review E*, 79(3):031926, 2009.

[28] Michael R Tonks, Amani Cheniour, and Larry Aagesen. How to apply the phase field method to model radiation damage. *Computational Materials Science*, 147:353–362, 2018.

[29] Dong-Uk Kim, Sophie Blondel, David E Bernholdt, Philip Roth, Fande Kong, David Andersson, Michael R Tonks, and Brian D Wirth. Modeling mesoscale fission gas behavior in UO_2 by directly coupling the phase field method to spatially resolved cluster dynamics. *Materials Theory*, 6(1):1–28, 2022.

[30] Larry K Aagesen, Daniel Schwen, Michael R Tonks, and Yongfeng Zhang. Phase-field modeling of fission gas bubble growth on grain boundaries and triple junctions in UO_2 nuclear fuel. *Computational Materials Science*, 161:35–45, 2019.

[31] Larry K Aagesen, Yipeng Gao, Daniel Schwen, and Karim Ahmed. Grand-potential-based phase-field model for multiple phases, grains, and chemical components. *Physical Review E*, 98(2):023309, 2018.

[32] Mathis Plapp. Unified derivation of phase-field models for alloy solidification from a grand-potential functional. *Physical Review E*, 84(3):031601, 2011.

[33] ROA Hall, MJ Mortimer, and DA Mortimer. Surface energy measurements on UO_2-a critical review. *Journal of Nuclear Materials*, 148(3):237–256, 1987.

[34] Hansjoachim Matzke. Atomic transport properties in UO_2 and mixed oxides $(U, Pu)O_2$. *Journal of the Chemical Society, Faraday Transactions 2: Molecular and Chemical Physics*, 83(7):1121–1142, 1987.

[35] Cody J Permann, Michael R Tonks, Bradley Fromm, and Derek R Gaston. Order parameter re-mapping algorithm for 3d phase field model of grain growth using fem. *Computational Materials Science*, 115:18–25, 2016.

[36] Tomohiro Takaki, Tomoyuki Hirouchi, Yousuke Hisakuni, Akinori Yamanaka, and Yoshihiro Tomita. Multi-phase-field model to simulate microstructure evolutions during dynamic recrystallization. *Materials transactions*, 49(11):2559–2565, 2008.

[37] J and-P Crocombette, F Jollet, L Thien Nga, and T Petit. Plane-wave pseudopotential study of point defects in uranium dioxide. *Physical Review B*, 64(10):104107, 2001.

[38] Pankaj V Nerikar, Xiang-Yang Liu, Blas P Uberuaga, CR Stanek, SR Phillpot, and SB Sinnott. Thermodynamics of fission products in $UO_2 \pm x$. *Journal of Physics: Condensed Matter*, 21(43):435602, 2009.

[39] M Idiri, T Le Bihan, S Heathman, and J Rebizant. Behavior of actinide dioxides under pressure: UO_2 and ThO_2. *Physical Review B*, 70(1):014113, 2004.

[40] JB Ainscough, BW Oldfield, and JO Ware. Isothermal grain growth kinetics in sintered UO_2 pellets. *Journal of Nuclear Materials*, 49(2):117–128, 1973.

[41] Pankaj V Nerikar, Karin Rudman, Tapan G Desai, Darrin Byler, Cetin Unal, Kenneth J McClellan, Simon R Phillpot, Susan B Sinnott, Pedro Peralta, Blas P Uberuaga, et al. Grain boundaries in uranium dioxide: scanning electron microscopy experiments and atomistic simulations. *Journal of the American Ceramic Society*, 94(6):1893–1900, 2011.

[42] Derek R. Gaston, Cody J. Permann, John W. Peterson, Andrew E. Slaughter, David Andrš, Yaqi Wang, Michael P. Short, Danielle M. Perez, Michael R. Tonks, Javier Ortensi, Ling Zou, and Richard C. Martineau. Physics-based multiscale coupling for full core nuclear reactor simulation. *Annals of Nuclear Energy*, 84:45–54, 2015.

[43] Z. Wallen. Heat generation rates of minifuel experiment assembly in removable beryllium position 5b of hfir. Technical Report C-HFIR-2021-021, Oak Ridge National Laboratory, Oak Ridge, TN, USA, March 2022.

[44] CT Walker, T Kameyama, S Kitajima, and M Kinoshita. Concerning the microstructure changes that occur at the surface of UO_2 pellets on irradiation to high burnup. *Journal of nuclear materials*, 188:73–79, 1992.

[45] C.T. Walker, V.V. Rondinella, D. Papaioannou, S. Van Winckel, W. Goll, and R. Manzel. On the oxidation state of UO_2 nuclear fuel at a burn-up of around 100MWd/kgHM. *Journal of Nuclear Materials*, 345(2):192–205, 2005.

[46] H. Kleykamp. Iaea specialists meeting on internal fuel rod chemistry. *IWGPFT/3*, 1979. Cited by: 3.

[47] MG Adamson, EA Aitken, SK Evans, and JH Davies. Oxygen redistribution and its measurement in irradiated oxide fuels. Technical report, General Electric Co., Pleasanton, Calif.(USA). Vallecitos Nuclear Center, 1975.

[48] Katsumi Une, Yasuo Tominaga, and Shinji Kashibe. Oxygen potentials and lattice parameter of irradiated bwr fuek. *Journal of Nuclear Science and Technology*, 28(5):409–417, 1991.